The tidal history of Iapetus: Spin dynamics in the light of a refined dissipation model

Julie C. Castillo-Rogez,[1] Michael Efroimsky,[2] and Valéry Lainey[3]

[1]   We study the tidal history of an icy moon, basing our approach on a dissipation model, which combines viscoelasticity with anelasticity and takes into account the microphysics of attenuation. We apply this approach to Iapetus, the most remote large icy moon in the Saturnian system. Different authors provide very different estimates for Iapetus's despinning timescale, by several orders of magnitude. One reason for these differences is the choice of the dissipation model used for computing the spin evolution. As laboratory data on viscoelastic properties of planetary ices are sparse, many studies relied on dissipation models that turned out to be inconsistent with experiment. A pure water ice composition, generally assumed in the previous studies of the kind, yields despinning times of the order of 3.7 Gyr for most initial conditions. We demonstrate that through accounting for the complexity of the material (like second-phase impurities) one arrives at despinning times as short as 0.9 Gyr. A more exact estimate will remain unavailable until we learn more about the influence of impurities on ice dissipation. By including the triaxial-shape-caused torque, we encounter a chaotic behavior at the final stage of despinning, with the possibility of entrapments in the intermediate resonances. The duration of these entrapments turns out to be sensitive to the dissipation model. No long entrapments have been found for Iapetus described with our laboratory-based dissipation model.

1.   Motivation

[2]   With its albedo dichotomy, the largest nonhydrostatic oblateness observed in the Solar system, a 20 km high and 150 km wide equatorial ridge, an almost 8° inclination to Saturn's equator (and, accordingly, to the orbits of other large Saturnian moons), Iapetus is one of the most puzzling objects of the Solar System.

[3]   Although currently Iapetus is locked in a 1:1 spin-orbit resonance with Saturn and rotates at a period of 79.33 days, its original state was most likely one of more rapid rotation, as can be deduced from Iapetus' shape. The 33 km difference between its equatorial and polar radii [*Thomas et al.*, 2007] has been interpreted as the fossil shape of the satellite when its spin period was between 15 and 16 h [*Castillo-Rogez et al.*, 2007] Theoretical models of satellite accretion (summarized by *Castillo-Rogez et al.* [2007]) suggest that the spin period at the end of accretion could be as short as 7 to 10 h.

[4]   Most large moons of the giant planets are believed to have achieved the 1:1 spin-orbit resonance with their primaries not long after formation. The despinning time of a satellite scales as its distance to the planet, to the minus sixth power, and is normally expected to lie within hundreds of thousands to several millions of years.

[5]   Assuming a constant quality factor Q equal to 100, *Peale* [1977] obtained for Iapetus' a tidal despinning time of order 10 Ga, much longer than for other large moons. As demonstrated by *Aleshkina* [2009], the use of a dissipation model with Q inversely proportional to the tidal frequency inflates the despinning time by two more orders of magnitude. Under the initial conditions chosen by *Aleshkina* [2009], Iapetus traverses the low-order resonances nonstop. At the same time, it was acknowledged by *Aleshkina* [2009] that different initial conditions might cause a temporary capture in some of the resonances, in which case the despinning timescale would be even longer.

[6]   The construction of more adequate models of tidal dissipation in Iapetus and other satellites is thus needed. First and foremost, these models should include the actual dependence of the damping rate upon the tidal frequency. As demonstrated by *Efroimsky and Lainey* [2007], employment of a realistic dissipation law based on experimental measurements can considerably influence the timescale of dynamical evolution of the Solar system objects and is also relevant to exoplanetary systems. At a more comprehensive level, a model should also account for the feedback between the thermodynamical state and the forcing stress and frequency. For example, many minerals (including ices) are

[1]Jet Propulsion Laboratory, California Institute of Technology, Pasadena, California, USA.
[2]U.S. Naval Observatory, Washington, D. C., USA.
[3]IMCCE, Observatoire de Paris, UMR 8028 du CNRS, Paris, France.

Report Documentation Page

*Form Approved
OMB No. 0704-0188*

Public reporting burden for the collection of information is estimated to average 1 hour per response, including the time for reviewing instructions, searching existing data sources, gathering and maintaining the data needed, and completing and reviewing the collection of information. Send comments regarding this burden estimate or any other aspect of this collection of information, including suggestions for reducing this burden, to Washington Headquarters Services, Directorate for Information Operations and Reports, 1215 Jefferson Davis Highway, Suite 1204, Arlington VA 22202-4302. Respondents should be aware that notwithstanding any other provision of law, no person shall be subject to a penalty for failing to comply with a collection of information if it does not display a currently valid OMB control number.

1. REPORT DATE **2011**	2. REPORT TYPE	3. DATES COVERED **00-00-2011 to 00-00-2011**

4. TITLE AND SUBTITLE **The Tidal History Of Iapetus: Spin Dynamics In The Light Of A Refined Dissipation Model**	5a. CONTRACT NUMBER
	5b. GRANT NUMBER
	5c. PROGRAM ELEMENT NUMBER
6. AUTHOR(S)	5d. PROJECT NUMBER
	5e. TASK NUMBER
	5f. WORK UNIT NUMBER
7. PERFORMING ORGANIZATION NAME(S) AND ADDRESS(ES) **U.S. Naval Observatory,Washington,DC,20007**	8. PERFORMING ORGANIZATION REPORT NUMBER
9. SPONSORING/MONITORING AGENCY NAME(S) AND ADDRESS(ES)	10. SPONSOR/MONITOR'S ACRONYM(S)
	11. SPONSOR/MONITOR'S REPORT NUMBER(S)

12. DISTRIBUTION/AVAILABILITY STATEMENT
Approved for public release; distribution unlimited

13. SUPPLEMENTARY NOTES
JOURNAL OF GEOPHYSICAL RESEARCH, VOL. 116,2011

14. ABSTRACT

15. SUBJECT TERMS

16. SECURITY CLASSIFICATION OF:			17. LIMITATION OF ABSTRACT	18. NUMBER OF PAGES	19a. NAME OF RESPONSIBLE PERSON
a. REPORT **unclassified**	b. ABSTRACT **unclassified**	c. THIS PAGE **unclassified**	**Same as Report (SAR)**	**29**	

Standard Form 298 (Rev. 8-98)
Prescribed by ANSI Std Z39-18

known to become more dissipative with increasing temperature (i.e., with decreasing viscosity).

2. Statement of Purpose

[7] Behavior of icy moons under high tidal stress, such as Europa or Enceladus (where the tidal stress is of the order of 10^5 Pa), has received much attention, since for these bodies tides are easily identified as a major driver of endogenic activity. At the same time, tidal dissipation and its impact on the internal evolution of objects subject to very low stressing still await exploration. This is why we address Iapetus, an icy moon experiencing tidal stresses of the order of 10^2 Pa.

[8] We construct a new dissipation model which rests on our laboratory-based understanding of the viscoelastic properties of ice. While no attenuation measurements on icy materials have yet been obtained under conditions exactly identical to those on Iapetus, our approach is based on a large bulk of relevant experimental observations and theoretical considerations available by now. The approach includes quantifying the friction rate as a function of the deformation mechanisms expected to act in Iapetus under the assumption of low porosity. In our computations, we trace the time evolution of the temperature and the excitation frequency, and thereby of the viscoelastic properties of the material. Our simulations are based on the despinning theory developed by *Efroimsky and Williams* [2009], combined with the geophysical model by *Castillo-Rogez et al.* [2007]. Specifically, we amend that model with a realistic dissipation law which relies on experimental measurements. We also consider the effect of Iapetus' triaxial shape (triaxiality) on despinning. Finally, we explore the important question of the evolution of the tidal torque on approach to a spin-orbit resonance.

[9] In section 3, we recall the meaning of linearity and discuss the frequency dependencies of the quality factor, tidal Love numbers, and phase lag. In section 4, we present a formula for the tidal-despinning rate. Section 5 summarizes the previously performed research on Iapetus' tidal despinning. Section 6 discusses the rationale for introducing a new dissipation model consistent with the temperature and stress conditions expected in Iapetus, supported by geophysical considerations. In section 7, we assemble our model in its entirety and present the results of numerical calculations. We also probe the possible role of the triaxiality. Conclusions are drawn in section 8. In Appendix A, we explain why the realistic dissipation models (with Q scaling as a positive power of frequency) do not entail infinities in the expressions for the tidal torque. We thus refute a popular fallacy that such rheologies yield diverging torques in the zero-frequency limit.

3. The Quality Factor, Phase Lag, and Love Numbers

3.1. Tidal Deformation of a Homogeneous Spherical Primary

[10] A stationary potential $W(\mathbf{R}, \mathbf{R}^*)$, generated by a secondary residing at $\mathbf{R}^*$ outside the primary, can be expanded, at each point $\mathbf{R}$ on the primary's surface, over the Legendre polynomials $P_l(\cos\gamma)$. Here γ denotes the angular separation between $\mathbf{R}^*$ and $\mathbf{R}$, both vectors coming out of the primary's center. Stationary deformation is linear if in the expansion

each tidal change of the potential, W_l, entails a linearly proportional deformation of the primary's shape. The deformation will, in its turn, amend the potential of the primary with a linear adjustment U_l:

$$U_l(\mathrm{R}) \sim W_l(\mathrm{R}, \mathrm{R}^*). \tag{1}$$

[11] For a spherical primary with mean equatorial radius R, the potential at degree l decreases outside the surface as $1/r^{l+1}$. Hence, the linearity assertion results in

$$U_l(\mathrm{R}) = k_l \left(\frac{R}{r}\right)^{l+1} W_l(\mathrm{R}, \mathrm{R}^*), \tag{2}$$

k_l being the Love number, $\mathbf{R}^* = (r^*, \phi^*, \lambda^*)$ being the radius, latitude, and longitude of the tide-raising secondary, $\mathbf{r} = (R, \phi, \lambda)$ being the coordinates of a surface point, and $\mathbf{r} = (r, \phi, \lambda)$ being those of an exterior point located above it at a radius $r \geq R$.

[12] Leaving consideration of radially stratified objects for section 3.5, we begin with the simpler case of homogeneous bodies. For a homogeneous incompressible spherical primary of density ρ, surface gravity g, radius R, and static rigidity μ (or the static compliance $J = 1/\mu$), the static quadrupole Love number is given by [*MacDonald*, 1964]

$$k_2 = \frac{3}{2} \frac{1}{1 + A_2}, \quad \text{where} \quad A_2 \equiv \frac{19}{2} \frac{\mu}{\rho\, \mathrm{g}\, R} = \frac{57\, \mu}{8\, \pi\, \gamma\, \rho^2\, R^2}$$

$$= \frac{57\, J^{-1}}{8\, \pi\, \gamma\, \rho^2\, R^2}, \tag{3}$$

$\gamma = 6.7 \times 10^{-11}$ m^3 kg^{-1} s^{-2} being Newton's gravity constant. For an arbitrary l, the general formula is:

$$k_l = \frac{3}{2(l-1)} \frac{1}{1 + A_l}, \quad \text{where} \quad A_l \equiv \frac{(2l^2 + 4l + 3)\mu}{l\, \mathrm{g}\, \rho\, R}$$

$$= \frac{3(2l^2 + 4l + 3)\mu}{4\, l\, \pi\, G\, \rho^2\, R^2}. \tag{4}$$

[13] All the above pertains to stationary loads and, accordingly, static Love numbers. A realistic tide varies in time and can be expanded into modes given by expression (37) below. Historically, the modes ω_{lmpq} are numbered with four integers [*Kaula*, 1964]: $lmpq$, where $l \geq 2$. The modes' absolute values, $\chi_{lmpq} \equiv |\omega_{lmpq}|$, are the actual physical frequencies of stresses and, consequently, of strains. Due to internal friction, a spectral component of the strain lags behind the appropriate component of the stress by a frequency-dependent phase shift $\epsilon_{lmpq}(\chi)$, the functional form of the frequency dependence being different for different values of l but independent of m, p, q. This is why the customary notation ϵ_{lmpq} may be substituted with a notation depicting the situation more accurately: $\epsilon_l(\chi_{lmpq})$. The Love numbers $k_l(\chi_{lmpq})$, too, depend upon the frequency, the dependencies looking different for different ls and bearing no dependence upon m, p, q. (The situation changes in bodies of a triaxial shape. There, coupling between spherical harmonics renders the Love numbers and lags whose expressions via the frequency depend on m, p, q [*Dehant*, 1987a, 1987b; *Smith*, 1974].)

[14] To keep the model linear under varying load, we assume that for deformation at frequency χ_{lmpq}, the appropriate Love numbers $k_l(\chi_{lmpq})$ and lags $\epsilon_l(\chi_{lmpq})$ depend on χ_{lmpq}, and not on the other frequencies in the spectrum, nor on the deformation magnitude at this or other frequencies.

[15] When lagging is linear, the average dissipation rate $\langle \dot{E}(\chi) \rangle$ and a one-cycle energy loss $\Delta E_{cycle}(\chi)$ at a frequency χ can be expressed with the empirical relations

$$\langle \dot{E}(\chi) \rangle = -\chi \, \frac{E_{peak}(\chi)}{Q(\chi)} \quad \text{and} \quad \Delta E_{cycle}(\chi) = -2\,\pi\,\frac{E_{peak}(\chi)}{Q(\chi)}. \tag{5}$$

If $E_{peak}(\chi)$ is the peak energy stored at the frequency χ, the Q factor is related to the lag via

$$Q^{-1} = \sin|\epsilon| \tag{6}$$

and not $Q^{-1} = \tan|\epsilon|$ as often presumed. Indeed, the latter definition is widely used in the experimental literature but is not directly applicable in the present case. If $E_{peak}(\chi)$ is defined as the peak work, the corresponding Q factor will be related to the lag in a more complicated manner, as demonstrated by *Efroimsky and Williams* [2009]:

$$Q^{-1} = \frac{\tan|\epsilon|}{1 - \left(\frac{\pi}{2} - |\epsilon|\right)\tan|\epsilon|}. \tag{7}$$

[16] *Efroimsky and Williams* [2009] were inaccurate when they called $E_{peak}(\chi)$ the peak energy. However, their calculation of Q was carried out with the understanding that $E_{peak}(\chi)$ is the peak work.

[17] In the limit of small ϵ, expression (7) becomes

$$Q^{-1} = \sin|\epsilon| + O(\epsilon^2), \tag{8}$$

so definition (7) makes $1/Q$ a good approximation to $\sin\epsilon$ for small lags only.

[18] Both definitions also render $Q \to 0$ for $\epsilon \to \pi/2$.

[19] The Darwin-Kaula expansion of tides contains not the inverse quality factors, but sines of the phase lags (see, for example, formula (102) of *Efroimsky and Williams* [2009] or our formula (35)). Thus, the despinning theory used in this study will operate with $\sin\epsilon$ and not with $1/Q$, as the definition of Q is genuinely ambiguous.

[20] Getting back to the Love numbers, we would recall that a potential proportional to $P_l(\cos\gamma)$ must be decreasing outside the primary as $r^{-(l+1)}$. Then we see that the tidal dynamics is determined almost exclusively by the principal Love number k_2.

3.2. Complex Notations for the Stress, Strain, Rigidity, and Compliance

[21] Insofar as the linear approximation remains valid, the stress tensor $\sigma_{\zeta\nu}$ and the strain tensor $u_{\zeta\nu}$ can be expanded into Fourier series

$$\sigma_{\zeta\nu}(t) = \sum_{\chi} \mathcal{R}e\left[\overline{\sigma}_{\zeta\nu}(\chi)e^{i\chi t}\right], \qquad u_{\zeta\nu}(t) = \sum_{\chi} \mathcal{R}e\left[\overline{u}_{\zeta\nu}(\chi)e^{i\chi t}\right], \tag{9}$$

the complex amplitudes being:

$$\overline{\sigma}_{\zeta\nu}(\chi) = \sigma_{\zeta\nu}(\chi)\,e^{i\varphi_\sigma(\chi)}, \qquad \overline{u}_{\zeta\nu}(\chi) = u_{\zeta\nu}(\chi)\,e^{i\varphi_u(\chi)}. \tag{10}$$

[22] At each frequency χ, the initial phases $\varphi_\sigma(\chi)$ and $\varphi_u(\chi)$ can be picked so that the amplitudes $\sigma_{\zeta\nu}(\chi)$ and $u_{\zeta\nu}(\chi)$ are nonnegative.

[23] In the case of a continuous spectrum, the sums will become integrals:

$$\sigma_{\zeta\nu}(t) = \int_0^\infty \overline{\sigma}_{\zeta\nu}(\chi)\,e^{i\chi t}\,d\chi \quad \text{and} \quad u_{\zeta\nu}(t) = \int_0^\infty \overline{u}_{\zeta\nu}(\chi)\,e^{i\chi t}\,d\chi, \tag{11}$$

where we omit the symbol $\mathcal{R}e$ and, for evident physical reasons, integrate over positive χ only. Whenever necessary, the frequency will be assumed to approach the real axis from below: $\mathcal{I}m(\chi) < 0$, so (11) will be a Laplace rather than a Fourier transform.

[24] Under the assumption of incompressibility, the volumetric part of the strain is nil. Hence in what follows we shall deal only with the deviatoric components. In a linear material with memory, the strain is rendered by the compliance operator $\hat{J}(t)$:

$$2\,u_{\zeta\nu}(t) = \hat{J}(t)\,\sigma_{\zeta\nu} = \int_0^\infty J(\tau)\,\dot{\sigma}_{\zeta\nu}(t - \tau)\,d\tau$$
$$= \int_{-\infty}^t J(t - t')\,\dot{\sigma}_{\zeta\nu}(t')\,dt', \tag{12a}$$

the overdot denoting time derivative. The kernel $J(t - t')$, termed compliance function or creep response function [*Karato*, 2008], describes the mechanical behavior of a medium (i.e., its capacity to comply) in response to an applied stress, and thus characterizes its memory. A stress increment $d\sigma_{\zeta\nu}(t') = \dot{\sigma}_{\zeta\nu}(t')dt'$ at the time t' contributes to the strain at a later time as follows: $2du_{\zeta\nu}(t) = J(t - t')d\sigma_{\zeta\nu}(t')$.

[25] After integration by parts, the operator acquires the form of

$$2\,u_{\zeta\nu}(t) = \hat{J}(t)\,\sigma_{\zeta\nu} = J(0)\,\sigma_{\zeta\nu}(t) - J(\infty)\,\sigma_{\zeta\nu}(-\infty)$$
$$+ \int_{-\infty}^t \dot{J}(t - t')\,\sigma_{\zeta\nu}(t')\,dt' \tag{12b}$$

$$2\,u_{\zeta\nu}(t) = -J(\infty)\,\sigma_{\zeta\nu}(-\infty)$$
$$+ \int_{-\infty}^t \frac{d}{dt}\left[J(t - t') - J(0) + J(0)\,\Theta(t - t')\right]\sigma_{\zeta\nu}(t')\,dt', \tag{12c}$$

$\Theta(t - t')$ denoting the Heaviside step function, which vanishes for $t - t' < 0$ and assumes the value of unity for $t - t' \geq 0$.

[26] Assuming that the stress $\sigma_{\zeta\nu}(-\infty)$ infinitely long ago was zero, we drop the term containing the relaxed compliance $J(\infty)$. However, the unrelaxed compliance, $J(0)$, is always important, as it describes an immediate response to forcing. It can, though, be incorporated into the kernel. As we just saw in (12c), this can be done if we accept that the unrelaxed compliance enters the compliance function not as $J(t - t') =$

$J(0) + \ldots$ but as $J(t - t') = J(0)\Theta(t - t') + \ldots$. Hence, in what follows we shall always write

$$2\, u_{\zeta\nu}(t) = \int_{-\infty}^{t} \dot{J}(t - t')\, \sigma_{\zeta\nu}(t')\, dt'. \qquad (13)$$

implying that $J(t - t')$ includes $J(0)\,\Theta(t - t')$ instead of $J(0)$.

[27] Complementary to the shear compliance operator $\hat{J}(t)$ is the operator of shear stress relaxation $\hat{\mu}(t)$, which may as well be called the operator of rigidity:

$$\sigma_{\zeta\nu}(t) = 2\,\hat{\mu}(t)\, u_{\zeta\nu} = \int_{0}^{\infty} 2\,\mu(\tau)\, \dot{u}_{\zeta\nu}(t - \tau)\, d\tau$$
$$= \int_{-\infty}^{t} 2\,\mu(t - t')\, \dot{u}_{\zeta\nu}(t')\, dt'. \qquad (14)$$

Its kernel, $\mu(t - t')$, named the stress relaxation function, may include the term $\mu(0)\Theta(t - t')$ responsible for the elastic stress. Here $\mu(0)$ is the unrelaxed rigidity, an inverse to the unrelaxed compliance: $\mu(0) = 1/J(0)$. The kernel may also include the viscous term $2\eta\delta(t - t')$, with $\delta(t - t')$ denoting the delta function, and η being the viscosity.

[28] In the presence of viscosity, $\hat{\mu}$ thus becomes an integro-differential operator, and not an integral operator like $\hat{J}$. This makes the integration by parts like (12b) and (12c) impossible. Accordingly, we cannot write the stress as $\sigma_{\zeta\nu}(t) = 2\int_{-\infty}^{t} \dot{\mu}(t - t')u_{\zeta\nu}(t')dt'$.

[29] Introducing the complex compliance $\overline{J}(\chi)$ through

$$\int_{-\infty}^{\infty} \overline{J}(\chi)e^{i\chi\tau}d\chi = \dot{J}(\tau) \quad \text{where} \quad \overline{J}(\chi) = \int_{0}^{\infty} \dot{J}(\tau)e^{-i\chi\tau}d\tau, \qquad (15)$$

and defining the complex rigidity $\overline{\mu}(\chi)$ as

$$\overline{\mu}(\chi) \equiv 1/\overline{J}(\chi), \qquad (16)$$

one can interconnect the complex amplitudes (11) through

$$\overline{\sigma}_{\zeta\nu}(\chi) = 2\,\overline{\mu}(\chi)\,\overline{u}_{\zeta\nu}(\chi), \qquad 2\,\overline{u}_{\zeta\nu}(\chi) = \overline{J}(\chi)\,\overline{\sigma}_{\zeta\nu}(\chi). \qquad (17)$$

(The presence of the viscous term $2\eta\delta(t - t')$ in the kernel $\mu(t - t')$, prevents us from defining $\overline{\mu}(\chi)$ via

$$\int_{-\infty}^{\infty} \overline{\mu}(\chi)e^{i\chi\tau}d\chi = \dot{\mu}(\tau), \quad \text{where} \quad \overline{\mu}(\chi) = \int_{0}^{\infty} \dot{\mu}(\tau)e^{-i\chi\tau}d\tau,$$

lest we have to deal with a derivative of the delta function.) Writing the complex rigidity and compliance as

$$\overline{\mu}(\chi) = |\overline{\mu}(\chi)|\, \exp[\delta(\chi)] \quad \text{and} \quad \overline{J}(\chi) = |\overline{J}(\chi)|\, \exp[-\delta(\chi)], \qquad (18)$$

one obtains

$$\tan\delta(\chi) \equiv -\frac{\mathcal{I}m[\overline{J}(\chi)]}{\mathcal{R}e[\overline{J}(\chi)]} = \frac{\mathcal{I}m[\overline{\mu}(\chi)]}{\mathcal{R}e[\overline{\mu}(\chi)]}. \qquad (19)$$

Evidently, the phase angle $\delta(\chi)$ is a measure of lagging of the strain at the frequency χ behind the stress at this frequency:

$$\varphi_u(\chi) = \varphi_\sigma(\chi) - \delta(\chi). \qquad (20)$$

3.3. The Love Operators and the Complex Love Numbers

[30] Consider a homogeneous incompressible primary subject to a stationary disturbance by a secondary. The lth spherical harmonic of the disturbance-caused increment of the primary's exterior potential is traditionally denoted as $U_l(\boldsymbol{R})$. This increment is related to the lth spherical harmonic $W_l(\boldsymbol{R}, \boldsymbol{R})$ of the perturbing exterior potential via relation (2).

[31] For time-dependent deformations, the Love numbers become integral operators, so relation (2) must be generalized to

$$U_l(\mathrm{R}, t) = \left(\frac{R}{r}\right)^{l+1} \hat{k}_l(t)\, W_l(\mathrm{R}, \mathrm{R}^*, t'). \qquad (21)$$

Under weak deformations, it is natural to assume this operator to be linear, so

$$U_l(\mathrm{R}, t) = \left(\frac{R}{r}\right)^{l+1} \int_{0}^{\infty} k_l(\tau)\dot{W}_l(\mathrm{R}, \mathrm{R}^*, t - \tau)d\tau$$
$$= \left(\frac{R}{r}\right)^{l+1} \int_{-\infty}^{t} k_l(t - t')\dot{W}_l(\mathrm{R}, \mathrm{R}^*, t')dt'. \qquad (22a)$$

Integration by parts provides an equivalent expression:

$$U_l(\mathrm{R}, t) = \left(\frac{R}{r}\right)^{l+1} \int_{0}^{\infty} \dot{k}_l(\tau)W_l(\mathrm{R}, \mathrm{R}^*, t - \tau)d\tau$$
$$= \left(\frac{R}{r}\right)^{l+1} \int_{-\infty}^{t} \dot{k}_l(t - t')W_l(\mathrm{R}, \mathrm{R}^*, t')dt'. \qquad (22b)$$

Just as in expressions (12b)–(12c) for the compliance operator, in (22b) we obtain the boundary terms $k_l(0)W(t)$ and $-k_l(\infty)W(-\infty)$. While setting $W(-\infty) = 0$ justifies our neglect of the latter term, the former term may be absorbed into the kernel by incorporating $k_l(0)\Theta(t - t')$ into $k_l(t - t')$.

[32] Expressions (22) coincide with (2) in the limit of a perfectly elastic body. Indeed, in this case $k_l(t - t')$ contains nothing but the immediate reaction term $k_l(0)\Theta(t - t')$, while the derivative of k_l becomes: $\dot{k}_l(t - t') = k_l(0)\delta(t - t')$. Sometimes the time derivatives $\dot{k}_l(\tau)$ are called Love functions, a term coined by *Churkin* [1998].

[33] In terms of the complex spectral components of $\overline{U}_l(\chi)$ and $\overline{W}_l(\chi)$, one can rewrite (22) as

$$\overline{U}_l(\chi) = \overline{k}_l(\chi)\, \overline{W}_l(\chi), \qquad (23)$$

$\overline{k}_l(\chi)$ being related to $\dot{k}_l(\tau) = dk_l(\tau)/d\tau$ via

$$\dot{k}_l(\tau) = \int_{0}^{\infty} \overline{k}_l(\chi)\, e^{i\chi\tau}d\chi \qquad (24)$$

(the idea of making the Love number complex was pioneered, likely, by *Munk and MacDonald* [1960] and *Zschau* [1978]). Insofar as alternating deformation remains linear, it obeys the elastic-viscoelastic analogy, a correspondence principle that relates a solution of a linear viscoelastic boundary value problem to an analogous problem of elastic body mechanics, with the same initial and boundary conditions [*Haddad*, 1995]. As a result of this correspondence, the algebraic

equations for the Fourier (or Laplace) components of the strain and stress in the viscoelastic problem mimic the equations interconnecting the strain and stress in the appropriate elastic problem. On these grounds, the operational moduli can be manipulated algebraically in the same way as their elastic counterparts. For this reason, the complex Love numbers are linked to the complex rigidity in the same manner as the static Love numbers depend upon the static rigidity. This correspondence, however, remains in force insofar as the linearity condition is met. As explained in section 6, Iapetus meets this requirement: the tidal stress in it is low enough to keep deformation linear (the dissipation thus being dominated by diffusion of defects through the lattice, a linear mechanism). At the same time, the developed theory may be too crude for the icy satellites subject to tidal stress of magnitudes greater than ~0.1 MPa (e.g., Europa), inside which the nonlinear mechanisms of grain boundary sliding or of dislocation creep are likely to be dominant. The applicability of the correspondence principle to those objects remains questionable.

[34] According to the correspondence principle, the algebraic dependence of a complex Love number on the complex rigidity mimics the relation between their static counterparts. The quadrupole Love number of a homogeneous near-spherical body will look:

$$\bar{k}_2(\chi) = \frac{3}{2} \frac{1}{1 + \frac{19\,\bar{\mu}(\chi)}{2\,\rho\,\mathrm{g}\,R}} = \frac{3}{2} \frac{1}{1 + \frac{19\,\mu}{2\,\rho\,\mathrm{g}\,R}\,\frac{\bar{\mu}(\chi)}{\mu}} = \frac{3}{2} \frac{1}{1 + A_2\,\bar{\mu}(\chi)/\mu}$$

(25a)

or, in terms of the complex compliance:

$$\bar{k}_2(\chi) = \frac{3}{2} \frac{1}{1 + A_2\,J/\bar{J}(\chi)} = \frac{3}{2} \frac{\bar{J}(\chi)}{\bar{J}(\chi) + A_2\,J},$$

(25b)

where the dimensionless factor is given by

$$A_2 \equiv \frac{19\,\mu}{2\,\rho\,\mathrm{g}\,R} = \frac{57\,\mu}{8\,\pi\,\gamma\,\rho^2\,R^2} = \frac{57\,J^{-1}}{8\,\pi\,\gamma\,\rho^2\,R^2},$$

(26)

γ being Newton's gravity constant. Formally, this expression for A_2 coincides with its static counterpart (3). A difference, however, exists. While in (3) letters μ and J signified the static rigidity and compliance, in (26) they may stand for any benchmark values obeying $\mu = 1/J$. The reason for this is that the product $A_2 J$ entering (25) does not in fact depend upon J or μ. It may be reasonable to use the unrelaxed values $\mu = \mu(0)$ and $J = J(0)$. However, this choice will not be obligatory, because in some rheological models the unrelaxed moduli may be zero or infinite.

[35] For an arbitrary l, (25) will become:

$$\bar{k}_l(\chi) = \frac{3}{2(l-1)} \frac{1}{1 + A_l\,J/\bar{J}(\chi)} = \frac{3}{2(l-1)} \frac{\bar{J}(\chi)}{\bar{J}(\chi) + A_l\,J},$$

(27)

with the above caveat concerning the expression of A_l via μ or J.

[36] The complex Love number can be naturally written as

$$\bar{k}_l(\chi) = \mathcal{R}e[\bar{k}_l(\chi)] + i\,\mathcal{I}m[\bar{k}_l(\chi)] = |\bar{k}_l(\chi)|\,e^{-i\epsilon_l(\chi)}$$

(28)

where $\epsilon_l(\chi)$ is the phase lag at the tidal frequency χ. It is defined through

$$\tan \epsilon_l(\chi) \equiv -\frac{\mathcal{I}m[\bar{k}_l(\chi)]}{\mathcal{R}e[\bar{k}_l(\chi)]}$$

(29)

or, equivalently, through

$$|\bar{k}_l(\chi)|\,\sin \epsilon_l(\chi) = -\mathcal{I}m[\bar{k}_l(\chi)]$$
$$= \frac{3}{2(l-1)} \frac{-A_l\,J\,\mathcal{I}m[\bar{J}(\chi)]}{(\mathcal{R}e[\bar{J}(\chi)] + A_l\,J)^2 + (\mathcal{I}m[\bar{J}(\chi)])^2}.$$

(30)

The importance of this formula stems from the fact that the product $k_l \sin \epsilon_l = |\bar{k}_l(\chi)|\sin \epsilon_l(\chi)$ emerges in the Darwin-Kaula expansion for the tidal potential. Hence it is this product (and not k_l/Q) that enters the tidal force, torque, and dissipation rate. This circumstance paves the way from a dissipation model to the despinning history. Indeed, the dissipation model implies a certain dependency of $\bar{J}$ on the frequency χ. The form of this dependency defines the frequency dependence of the Love numbers, $k_l(\chi)$. The latter define, for each l, the functional form of the dependencies (30) which, in their turn, are directly employed in the tidal theory.

3.4. The Case of an Incompressible Homogeneous Body

[37] Iapetus' rigidity, being temperature- and porosity-dependent, is likely to have varied, over the satellite's history, within the range of $\mu \sim 4 \times 10^8$ to 4×10^9 Pa. If we model Iapetus with an incompressible and homogeneous sphere of density $\rho \approx 10^3$ kg m^{-3} and radius $R \approx 7.5 \times 10^5$ m, these numbers put the value of A_l within the interval of 25–250. This tells us that

$$A_l \frac{J}{|\bar{J}(\chi)|} \gg 1,$$

(31)

so we can approximate (27) with

$$\bar{k}_l(\chi) = \frac{3}{2} \frac{\bar{J}(\chi)}{\bar{J}(\chi) + A_l J} \approx \frac{3}{2} \frac{\bar{J}(\chi)}{A_l J} + O\left(|\bar{J}/(A_l J)|^2\right),$$

(32)

except in the closest vicinity of the resonance, where the tidal frequency χ approaches zero, and $\bar{J}$ diverges for some mechanical models, like, for example, for those of Maxwell or Andrade. (Recall that according to (26), the dimensionless factor A_l is inversely proportional to J, so the product $A_l J$ does not in fact depend upon J.)

[38] Whenever the approximate formula (32) is applicable, we can rewrite (29) as

$$\tan \epsilon_l(\chi) \equiv -\frac{\mathcal{I}m[\bar{k}_l(\chi)]}{\mathcal{R}e[\bar{k}_l(\chi)]} \approx -\frac{\mathcal{I}m[\bar{J}(\chi)]}{\mathcal{R}e[\bar{J}(\chi)]} = \tan \delta(\chi),$$

(33)

whence the phase lag of a tidal mode at frequency χ coincides with the phase lag in a sample:

$$\epsilon_l(\chi) \approx \delta(\chi) \qquad \text{for all } l,$$

(34)

provided χ is not too close to zero (i.e., we are not too close to a resonance). Stated alternatively, for χ not approaching zero too closely, the component $\bar{U}_l(\chi)$ of the primary's potential

variation lags behind the component $\bar{W}_l(\chi)$ of the perturbed potential by the same phase angle as the strain lags behind the stress at frequency χ in a sample of the material.

[39] Just as (30), so formulae (32) and (33) should be employed with an important caveat in mind. In reality, the potential $\bar{U}$ and therefore also $\bar{k}$ are functions not of the positively defined physical frequencies χ but of the tidal modes ω, which can be positive or negative. Our illegitimate use of χ instead of ω should be compensated through multiplying the lag $\epsilon_l(\chi_{lmpq})$, "by hand," with sgnω_{lmpq}. So, for example, (34) should actually look

$$\epsilon_l(\chi) \approx \delta(\chi)\mathrm{sgn}\ \omega.$$

Leaving the (somewhat tedious) mathematical elucidation of this fact to another paper, we would mention that from the viewpoint of physics, the need for the sign factor is clear. Indeed, both the lag ϵ_{lmpq} and the appropriate term of the torque should change their sign on crossing the lmpq commensurability (while the lag δ in the material should always stay positive, as the strain always falls behind the stress causing it).

[40] Condition (31) is obeyed insofar as changes of shape are determined solely by the material properties, and not by self-gravitation of the object. This condition therefore restricts the applicability realm of (34). An even tougher limitation stems from the fact that the above treatment relied on the homogeneity assumption. Realistic models of larger bodies must account for the radial variations in the material properties due to temperature gradients and possible compositional stratification. (Such stratification may emerge if, for example, an icy moon has undergone internal melting, with the ensuing chemical differentiation of the interior.) For Iapetus, thermal models suggest that compositional differentiation was limited [*Castillo-Rogez et al.*, 2007]. Still, the impact of thermal variations on the mechanical properties of the material was substantial enough. So we cannot directly employ (34) but instead have to derive the overall lag ϵ through integration over layers.

3.5. The Case of a Radially Heterogeneous Body

[41] The dissipative properties of layered objects are explored by numerical integration of the deformation propagation from the interior to the surface, over the layers of the body. In our computations, we relied on the model developed by *Takeuchi and Saito* [1972] for an incompressible near-spherical object. The incompressibility assumption is generally adopted in the literature [e.g., *Tobie et al.*, 2005] because compression plays only a minor role in the overall tidal response of a body.

[42] The overall phase lag ϵ is computed via integration of δ over the layers. Hence, ϵ becomes a function of the composition stratification, the physical structure (e.g., the porosity and the presence of a liquid layer), and the temperature distribution. Computation of ϵ includes computation of the profile of stresses and strains over the layers, the compliance properties of the medium in each layer being different (though always remaining linear (see section 6)).

[43] The global deformation is inferred from the equation of motion, as explained by *Takeuchi and Saito* [1972]. Historically, their method was developed to model a static elastic deformation of a multilayered body, so the radial functions and equation of motion of *Takeuchi and Saito* [1972] contained the static rigidity. Thanks to the correspondence principle, the method can be applied to varying loads too. The radial functions and equations of motion (as well as the constitutive equations) are then written in the frequency domain and thus contain either the complex rigidity $\bar{\mu}(\chi)$ or its inverse, the complex compliance $\bar{J}(\chi)$. The method remains agnostic of the viscoelastic model employed, insofar as the model remains linear so the correspondence principle work.

[44] The complex tidal Love numbers $\bar{k}_l(\chi)$ are determined from the radial functions integrated to the surface. Assuming that the body is spherically symmetric and isotropic (and that neither of these two assumptions is violated too badly by convection), the deformation vector **u** generated by the tidal potential can be expanded over the spherical functions Y_l^m multiplied by some functions of radius (the latter functions being different for different layers). Details of numerical solution of the resulting system of differential equations are given by *Tobie et al.* [2005].

[45] The difference between the thus obtained Love number for an idealized spherical object and the appropriate Love number for an actual, slightly triaxial object is of the order of the flattening [*Dehant*, 1987a, 1987b; *Smith*, 1974]. Taken the uncertainty in our knowledge of the physical parameters, a small nonsphericity can then be neglected.

4. Parameterization of the Despinning Rate

[46] While the *MacDonald* [1964] theory tacitly sets the quality factor inversely proportional to the frequency, the theory of *Darwin* [1879] and *Kaula* [1964] is general enough to accommodate an arbitrary dissipation model. In the following, we shall employ their theory and shall treat Iapetus as the primary and Saturn as the secondary. Our first step will be to bring in the conventional expression for despinning rate. As it is common to write this expression with the Q factor in the denominator, our second step will be to recall that in reality, $1/Q$ is but an approximation to the correct factor sin ϵ, as can be easily seen from equation (35). For sufficiently large Q, the approximation works. However, experimental data show that under the conditions expected in icy moons, the Q factor of ice can become close to and even lower than unity [e.g., *McCarthy et al.*, 2008]. Thus, while the approximation is justified for telluric bodies, it is not, generally, applicable to icy moons. So we shall have to stick to the phase lag ϵ.

[47] As the inverse quality factor is (up to 2π) the relative energy loss, one may enquire if the values of Q can at all be close to or below unity. For seismic waves (which are similar to an underdamped undriven oscillator), the answer is negative. It is, however, affirmative for tides, for these are similar to a driven (and, in some cases, overdamped) oscillator. The quality factor falling short of unity indicates that the eigenfrequencies get damped away during less than one vibration and that the motion continues only due to the driving force.

[48] Our third step will be to recall that ϵ is the lag between the reaction of the primary's shape and the external load. It is, however, the phase lag δ, whose frequency dependence is measured in the lab. As the body is multilayer, we cannot approximate ϵ with δ but will have to average over layers to

obtain the overall $-\mathcal{I}m[\bar{k}_l(\chi)] = k_l(\chi)\sin\epsilon_l(\chi)$ for the body as a whole.

4.1. Despinning Torques in the Darwin-Kaula Theory of Bodily Tides

[49] In the presence of only one secondary (here, Saturn) located at the position $\boldsymbol{r} = (r, \phi, \lambda)$ relative to the primary (here, Iapetus), the tidal torque acting on the primary reads

$$
\begin{aligned}
\mathcal{T} &= \sum_{l=2}^{\infty} 2\gamma M_{sec}^2 R^{2l+1} a^{-2l-2} \sum_{m=0}^{l} \frac{(l-m)!}{(l+m)!} m \sum_{p=0}^{l} F_{lmp}^2(i) \\
&\quad \cdot \sum_{q=-\infty}^{\infty} G_{lpq}^2(e) k_l \sin\epsilon_{lmpq} \ + \ \tilde{\mathcal{T}} \\
&= -\sum_{l=2}^{\infty} 2\gamma M_{sec}^2 R^{2l+1} a^{-2l-2} \sum_{m=0}^{l} \frac{(l-m)!}{(l+m)!} \ m \ \sum_{p=0}^{l} F_{lmp}^2(i) \\
&\quad \cdot \sum_{q=-\infty}^{\infty} G_{lpq}^2(e) \mathcal{I}m[\bar{k}_l(\epsilon_{lmpq})] + \tilde{\mathcal{T}},
\end{aligned}
\tag{35}
$$

M_{sec}^2 being the mass of the secondary (Saturn), the sum standing for the constant (independent from the mean anomaly $\mathcal{M}$) part of the torque, M_{sec}^2 being the mass of the tide-raising secondary (whose role in this setting is played by Saturn), and $\tilde{\mathcal{T}}$ denoting the oscillating part whose time average is zero. (Following *Kaula* [1964], we write: $k_l \sin\epsilon_{lmpq}$, though notation $k_l(\chi_{lmpq})\sin\epsilon_l(\chi_{lmpq})$ would be more logical, as k_l and ϵ_l are the absolute value and the negative phase of the complex-valued function $\bar{k}_l(\chi_{lmpq})$.) Here $F_{lmp}(i)$ are the inclination functions, while $G_{lpq}(e)$ are the eccentricity polynomials identical to the Hansen coefficients $X_{(l-2p+q)}^{(-l-1),(l-2p)}$. The Love numbers k_l are our $|\bar{k}_l(\chi)|$, while the phase lags are given by

$$
\epsilon_{lmpq} = \left[(l-2p)\dot{\omega} \ + \ (l-2p+q)\dot{\mathcal{M}} \ + \ m(\dot{\Omega} - \dot{\theta})\right]\Delta t_{lmpq},
\tag{36}
$$

where θ is the sidereal angle of the primary, $\dot{\theta}$ is its spin rate, Δt_{lmpq} is the time lag at the mode

$$
\omega_{lmpq} = (l-2p)\dot{\omega} \ + \ (l-2p \ + \ q)\dot{\mathcal{M}} \ + \ m(\dot{\Omega} - \dot{\theta}),
\tag{37}
$$

while $a, e, i, \omega, \Omega, \mathcal{M}$ stand for the orbital elements of the secondary: the semimajor axis, eccentricity, inclination, argument of the pericenter, longitude of the node, and mean anomaly. The actual, physical frequencies of deformation in the primary are given by

$$
\chi_{lmpq} = |\omega_{lmpq}| = |(l-2p)\dot{\omega} \ + \ (l-2p+q)\dot{\mathcal{M}} \ + \ m(\dot{\Omega} - \dot{\theta})|.
\tag{38}
$$

Below we shall neglect the precessions ($\dot{\Omega} \approx 0$, $\dot{\omega} \approx 0$), and shall assume that $\dot{\mathcal{M}} = \dot{\mathcal{M}}_0 + n \approx n$.

[50] A comprehensive derivation of (35)–(38) is given by *Efroimsky and Williams* [2009]. As each term in the sum (35) is proportional to $k_l \sin\epsilon_{lmpq} = |\bar{k}_l(\chi_{lmpq})|\sin\epsilon_l(\chi_{lmpq}) = -\mathcal{I}m[\bar{k}_l(\chi_{lmpq})]$, it would be incorrect to introduce the frequency dependencies of $\sin\epsilon_{lmpq}$ and $k_l \equiv |\bar{k}_l|$ separately. Both

must be derived from the expression for the complex Love number $\bar{J}_l(\chi_{lmpq})$, which in its turn is deduced from the frequency dependence $\bar{J}(\chi_{lmpq})$. In the case of a homogeneous body, the latter is rendered, for $l = 2$, by (25) and is often well approximated by (32).

4.2. The Formula for Despinning Rate and Its Limitations

[51] As evident from expansion (35), the contribution of tidal mode ω_{lmpq} to despinning is proportional to $k_l(\chi) \sin\epsilon_{lmpq}(\chi)$, where $\chi \equiv \chi_{lmpq} = |\omega_{lmpq}|$. The principal tidal mode

$$
\omega_{2200} \ = \ 2(n - \dot{\theta})
\tag{39}
$$

generates the physical flexure frequency

$$
\chi_{2200} = 2|n - \dot{\theta}| = 2(\dot{\theta} - n)
\tag{40}
$$

and the phase lag

$$
\epsilon_{2200} \ \equiv \omega_{2200}\Delta t_{2200} \ = \chi_{2200} \ \Delta t_{2200} \ \text{sgn} \ \omega_{2200}.
\tag{41}
$$

(We ignore the mode $lmpq = 2000$, because an $lmpq$ term of the torque (35) is proportional to m. Thence the said mode contributes nothing in the spin dynamics of the tidally distorted body. This mode, though, does influence the variations of the body's shape and, consequently, the dissipation rate.) While the despinning is going on, i.e., while $\dot{\theta} > n$, the tidal mode ω_{2200} remains negative, as can be seen from (39). Then the phase lag (41), too, remains negative, as the time lag Δt_{2200} is positively defined. Hence the imaginary part of the Love number, $\mathcal{I}m[\bar{k}_2(\chi_{2200})] = -k_2 \sin\epsilon_{2200}$, stays positive during the despinning. Naturally, the leading term of the constant part of the torque,

$$
\begin{aligned}
\mathcal{T}_{2200} \ &= \ \frac{3}{2}\gamma \ M_{sec}^2 \ R^5 \ a^{-6} \ k_2 \sin\epsilon_{2200} \\
&= \ \frac{3}{2}\ \gamma \ M_{sec}^2 R^5 a^{-6} \ k_2 \sin|\epsilon_{2200}|\text{sgn} \ \omega_{2200},
\end{aligned}
\tag{42}
$$

remains negative and thereby decelerating the spin. Here $\dot{\theta}$ is the primary's spin rate, while M_{sec} is the mass of the secondary. Recall that in our setting the role of the tidally distorted primary is played by the satellite (Iapetus), while the role of the tide-raising secondary is played by the planet (Saturn).

[52] The derivation of (42), provided by *Efroimsky and Williams* [2009] and other sources, has $k_2 \sin\epsilon_{2200}$ approximated with $k_2 Q_{2200}^{-1} \text{sgn} \ \omega_{2200}$. For Iapetus, we cannot afford this approximation because over some period of its history the Q factor becomes small and the difference between Q and $\sin|\epsilon|$ becomes considerable. Thus, we have to stick to using $k_2 \sin\epsilon_{2200}$.

[53] Let us introduce the maximal moment of inertia of the primary (Iapetus):

$$
C \ = \ \xi \ M_{prim} \ R^2.
\tag{43}
$$

M_{prim} and R being the primary's mass and radius, and ξ being a numerical factor (equal to $\xi = 2/5$ for homogeneous spherical bodies). Then, in the accepted approximation, the

despinning rate will be given by

$$\ddot{\theta} = \frac{3}{2} \frac{\gamma}{\xi} \frac{M_{sec}^2}{M_{prim}} R^3 a^{-6} k_2 \sin|\epsilon_{2200}| \mathrm{sgn}\ \omega_{2200} + O(e^2 \sin \epsilon)$$
$$+ O(i^2 \sin \epsilon) \qquad (44\mathrm{a})$$

or, in terms of the mean motion $n = \sqrt{\gamma(M_{prim} + M_{sec})a^{-3}}$, by

$$\ddot{\theta} = \frac{3}{2} \frac{n^2 M_{sec}^2}{\xi M_{prim}(M_{prim} + M_{sec})} \left(\frac{R}{a}\right)^3 k_2 \sin|\epsilon_{2200}| \mathrm{sgn}\ \omega_{2200}$$
$$+ O(e^2 \sin \epsilon) + O(i^2 \sin \epsilon) = \frac{3}{2\xi} \frac{n^2 M_{sec}}{M_{prim}} \left(\frac{R}{a}\right)^3$$
$$\cdot k_2 \sin|\epsilon_{2200}| \mathrm{sgn}\ \omega_{2200} + O(e^2 \sin \epsilon) + O(i^2 \sin \epsilon)$$
$$+ O(M_{prim}/M_{sec}), \qquad (44\mathrm{b})$$

where we recalled that $M_{prim} \equiv M_{Iapetus} \ll M_{sec} \equiv M_{Saturn}$. As follows from (39), during the despinning process the sign of the principal tidal mode is negative: $\mathrm{sgn}\ \omega_{2200} = -1$. The value of $\sin|\epsilon_{2200}|$ is obtained by integration over layers, as explained in section 3.5.

[54] In the approximation of a homogeneous primary (and in understanding that $\sin \epsilon = \epsilon + O(\epsilon^2)$ and $\mathrm{sgn}\ \omega = -1$), expression (44) acquires the simple form of

$$\ddot{\theta} = -(\dot{\theta} - n)\mathcal{K} + O(e^2\epsilon) + O(i^2\epsilon) + O(\epsilon^2). \qquad (45)$$

where

$$\mathcal{K} = -3 \frac{\gamma}{\xi} \frac{M_{sec}^2}{M_{prim}} \frac{R^3}{a^6} k_2\ \Delta t_{2200}$$
$$= -\frac{3}{\xi} \frac{n^2 M_{sec}^2}{M_{prim}(M_{prim} + M_{sec})} \left(\frac{R}{a}\right)^3 k_2\ \Delta t_{2200}. \qquad (46)$$

However, this simplification is deceptive because, to implement it in practice, one still has to calculate the frequency dependence of $k_2\ \Delta t_{2200}$. Based on the dependence of the complex Love number upon the complex compliance, such a calculation provides the answer in the form of $k_2 \sin \epsilon_{2200} = |\bar{k}_2(\chi_{2200})| \sin \epsilon_2 (\chi_{2200}) = -\mathcal{I}m[\bar{k}_2(\chi_{2200})]$ anyway.

5. Some Previous Works on Iapetus' Tidal Despinning

5.1. Peale [1977] and Aleshkina [2009]

[55] The simplest approach to despinning is to assume that both k_2 and Q are constant. Using the standardized language of the empirical power law $Q \sim (\mathcal{E}\chi)^p$, where $\mathcal{E}$ is a constant having dimensions of time, we can express the said choice as

$$k_2(\chi) = \mathrm{const}, \qquad (47\mathrm{a})$$

$$Q \sim (\mathcal{E}\chi)^p, \quad \text{where}\quad p = 0. \qquad (47\mathrm{b})$$

[56] This way, the temperature and frequency dependencies and a lot of other physics get ignored. Within this approach, Peale [1977] explored despinning of the large moons in the solar system. Setting $Q = 100$, for Iapetus, Peale obtained a despinning time of about 10 Ga, which was much longer than for other large satellites.

[57] Following Peale [1977], Aleshkina [2009] set the Love number constant. In her dynamical simulations, Aleshkina [2009] employed the so-called modified MacDonald torque, i.e., the MacDonald [1964] empirical model amended with an assumption that for all tidal frequencies χ the appropriate time lags are equal to the same quantity $\mathcal{E}$:

$$\Delta t (\chi) = \mathcal{E}, \qquad (48)$$

whence the tidal Q scales as inverse frequency χ. All in all:

$$k_2(\chi) = \mathrm{const}, \qquad (49\mathrm{a})$$

$$Q \sim (\mathcal{E}\chi)^p, \quad \text{where}\quad p = -1. \qquad (49\mathrm{b})$$

[58] The empirical theory of bodily tides proposed by Gerstenkorn [1955] and furthered by MacDonald [1964] suffered an inherent inconsistency, because it treated the tidal quality factor Q as a constant. The empirical theory becomes equivalent to the rigorous development by Darwin [1879, 1880] and Kaula [1964] only for materials whose time lag and Q factor scale as (48) and (49b), correspondingly [Efroimsky and Williams, 2009]. From this viewpoint, the use of (49b) was justified. Unfortunately, though, (48) and (49) are incompatible with the actual properties of solids. This explains why employment of these formulae led to an implausibly long despinning.

5.2. Castillo-Rogez et al. [2007]

[59] Castillo-Rogez et al. [2007] pointed out that for Iapetus to despin over the Solar system age, its quality factor averaged over that entire time span must have been less than 70 (for $k_2 \sim 10^{-3}$). This value is relatively low. To obtain it within the model used by Castillo-Rogez et al. [2007], the internal temperature of the moon ought to have reached at least 263 K, i.e., to have approached the water-ice melting point. As was demonstrated by Castillo-Rogez et al. [2007], this might be achievable due to the insulating effect of porosity. However, a high porosity is compatible neither with freezing of the fossil equatorial bulge, nor with the expected high temperature of the interior. To compensate for the low porosity, Castillo-Rogez et al. [2007] suggested that heating due to the decay of short-lived radioisotopes, mainly ^{26}Al, could drive early compaction. The consequent increase in thermal conductivity would then justify the use of a colder model with a rapidly thickening lithosphere and with the deep interior still capable of reaching temperatures high enough to promote dissipation and despinning.

[60] While sufficiently comprehensive, the combined geophysical and dynamical calculation by Castillo-Rogez et al. [2007] suffered two drawbacks. First, it relied on a simplistic dissipation model, the one by Maxwell. Second, Castillo-Rogez et al. [2007] did not include convection. As convection is initiated, it prevents further warming of the interior. This problem was tackled later on by Robuchon et al. [2010].

5.3. Robuchon et al. [2010]

[61] Keeping some of the assumptions used by Castillo-Rogez et al. [2007] and introducing two major upgrades, Robuchon et al. [2010] recently developed a new model of Iapetus. The first upgrade was a block modeling convective
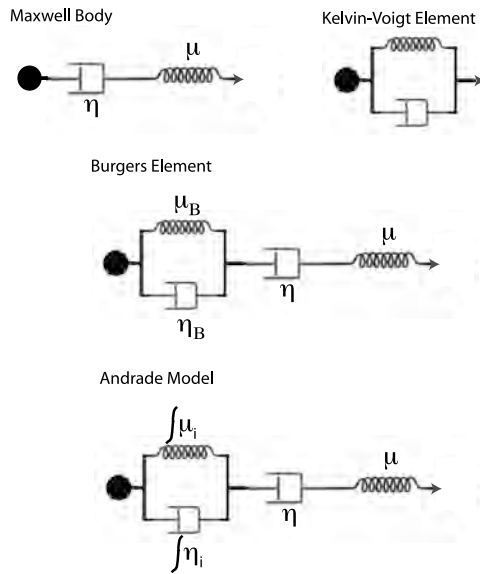
Figure 1. Schematic representation of various viscoelastic and anelastic models. A model is illustrated by an assemblage of springs and dashpots. Springs (labeled with μ) are aimed to represent the elastic properties of the medium, while dashpots (denoted with η) stand for the viscous properties. In the Burgers model, anelasticy is represented by one Voigt element, which is characterized by its specific elastic modulus and viscosity. In the case of the Andrade model, the anelastic component represents an infinite number of dashpots in series in parallel with an infinite number of springs and represents a continuous distribution of compliances and thus relaxation times.

heat transfer. They demonstrated that convection can start at temperatures lower than the optimum temperature necessary to achieve significant dissipation in the Maxwell model. As a second upgrade, they resorted to a different dissipation model, the Burgers element, in order to determine whether or not a dissipation rate leading to despinning can be achieved at low temperature. The Burgers element, illustrated by Figure 1, should not to be confused with the so-called extended Burgers model, which presents a more complex distribution of relaxation times. Resorting to the Burgers element was based on the observation by *Reeh et al.* [2003] that the model can reproduce the bending of floating glaciers in response to ocean tides. Applying the model to Iapetus, *Robuchon et al.* [2010] tested different values for the viscous and elastic moduli characterizing the transient response (between elastic behavior and viscous creep) in order to find a combination that could lead to a dissipative interior despite convection onset. They did find successful models in which dissipation could occur at temperatures as low as 200 K and in few hundred million years. This way, *Robuchon et al.*'s [2010] study was a pioneer attempt to take into account the anelastic response of ice in a tidal dissipation model. At the same time, it should be pointed out that the choice of the Burgers model by *Robuchon et al.* [2010] suffers the same flaws as the choice of the Maxwell model. Indeed, there exists a considerable discrepancy between the Burgers element and experimental results [*Jellinek and Brill*,

1956; *Tatibouet et al.*, 1987; *Jackson*, 1993; *Cole*, 1995; *Cooper*, 2002]. The reason for this is that attenuation is driven by the motion of defects whose geometry and distribution are complex and cannot be accounted for by a single Voigt element.

[62] We do not question the fact that the Burgers model did provide a good match to the observations of *Reeh et al.* [2003]. However, as pointed out by *Sohl and Spohn* [1997], who aimed to interpret Mars' tidal Love number and dissipation factor at the period of the forcing frequency exerted by Phobos, both the Maxwell model and the Burgers element can yield a result consistent with that observation. However, these different models imply different values for the viscosity of Mars' mantle. Thus, in principle, a single observational constraint may be interpreted via several possible dissipation models, which questions the geophysical meaning of the input parameters to these models.

[63] Besides, forward modeling of planetary dissipation involves a different set of issues. For one, the input parameters to the Burgers model (for the transient creep) inferred for Earth's cryosphere or mantle are not necessarily applicable to other bodies. The values inferred for Earth are for specific conditions of stress and temperature that are far different from those expected in Iapetus or other icy satellites: a temperature of $-30°C$ in the case of the *Reeh et al.* [2003] study [after *Brill and Camp*, 1961] and also a stress of a few hundred kilopascals. Thus, the extrapolation of the Burgers model to planetary bodies is not straightforward. *Robuchon et al.* [2010] varied the possible parameters of the transient Burgers element before finding the combinations that lead to despinning. As explained in section 6, the transient and steady state responses are necessarily coupled since, in the low-stress conditions relevant to Iapetus' despinning, they both involve the same defects.

[64] As a summary, since the experimental data on attenuation in silicates and other materials do not fit the Burgers element well, we would use caution when applying that model.

6. What Tidal Friction Model for Iapetus?

6.1. On the Limitations of "Tin Toys Models"

[65] Numerous studies assume planetary materials to behave as a Maxwell body, a model represented by a purely viscous damper and a purely elastic spring connected in series. The model was applied, for example, to a variety of icy satellites [e.g., *Tobie et al.*, 2005; *Castillo-Rogez et al.*, 2007]. The Maxwell model entails the following expression for the phase lag:

$$\tan \delta(\chi) \sim \frac{1}{\chi} \qquad (50)$$

χ being the frequency. Being unable to account for the anelastic behavior observed in planetary materials [*Cooper*, 2002], the model fails to account correctly for attenuation in minerals (see *Karato* [2008] for a detailed study, or *Efroimsky and Lainey* [2007] for a very brief review).

[66] As discussed below in more detail, numerous laboratory measurements indicate that the transient response of planetary materials is complex, and cannot be simply

accounted for by a discrete set of relaxation peaks. An adequate description requires a complicated distribution function of the relaxation time [e.g., *Jackson et al.*, 2002; *Cooper*, 2002]. The reason for broadening of the relaxation peak, compared to the Debye peaks characterizing the Maxwell body or the Burgers element, is that in realistic materials the defects driving dissipation (e.g., grain boundaries or dislocations) are not homogeneously distributed in the material. Besides this, the defects' parameters (e.g., dislocations lengths or grain shapes) may vary by orders of magnitude within one icy shell. These circumstances complicate the picture, and make simplistic tin toys models (i.e., assemblages of springs and dashpots) insufficient.

6.2. The "Elbow" Dependence and the Andrade Model

[67] Experimental exploration of attenuation in planetary materials began in the middle of the 20th century. In application to minerals, this research was motivated by the need to interpret seismic data. In application to ices, it was motivated by the interest in the mechanical properties of ice shelves; so the pioneering data were obtained from observing the transition from elastic deformation to steady state creep (e. g., to the primary creep of ice under a constant load). We refer the reader to *McCarthy and Castillo-Rogez* [2011] for details on the history of research on the dissipative properties in ices.

[68] These measurements demonstrate that the slope of the attenuation spectrum undergoes a drastic change at a threshold frequency that marks the boundary between a low-frequency and high-frequency regime (see *Efroimsky and Lainey* [2007] for a review).

[69] This entails, as a possible option, the following frequency dependence:

$$Q^{-1} = \tan \delta = (\mathcal{E} \, \chi)^{-p}, \text{ where } p = 0.2 - 0.4$$
$$\text{for } \chi \gg \chi_0 \text{ and } p = \sim 1.0 \text{ for } \chi \ll \chi_0, \qquad (51)$$

The empirical parameter $\mathcal{E}$ has the dimensions of time, and has the physical meaning of the average timescale associated with the dominating dissipation mechanism. As different mechanisms may dominate over different ranges of frequencies, both $\mathcal{E}$ and p can bear dependence on χ, but these dependencies are assumed to be slow, except for the fast change of p at the threshold frequency $\chi = \chi_0$.

[70] Evidence for the applicability of (51) at high frequencies comes from measurements in a lab [e.g., *Gribb and Cooper*, 1998; *Jackson et al.*, 2002] and seismic data [*Shito et al.*, 2004]. For ices, such behavior has been reported, for example, by *Cole* [1990]. Observational evidence for the low-frequency band comes from observation of the Chandler wobble and of the mantle's response to postglacial rebound [*Romanowicz and Durek*, 2000; *Karato and Spetzler*, 1990]. The change in the frequency dependence indicates that the attenuation in the material is dominated at low frequencies by its viscous properties [*Karato*, 2008], while at higher frequencies it is dominated by anelasticity [e.g., *Jackson et al.*, 2002].

[71] Several experimental studies have demonstrated that the change in regime is not immediate but involves a transitional region [e.g., *Jackson et al.*, 2002]. *Jackson et al.* [2002] also demonstrated on theoretical grounds that in the case of

grain boundary diffusion, the adjustment between the two regimes occurs on a timescale that is a function of the microstructural and viscoelastic properties of the material. However, further experimental and theoretical studies are needed in order to characterize the threshold χ_0.

[72] Analysis of numerous forced oscillation experiments indicate that the models, which include a broad relaxation term (such as the Andrade model or the extended Burgers model), provide the best fit to experimental data [e.g., *Tan et al.*, 2001; *Jackson et al.*, 2002; *Cooper*, 2002].

[73] Over the past years, the model pioneered by *Andrade* [1910, 1914] has been reported match for a variety of materials, over a wide range of experimental conditions [*Cottrell and Aytakin*, 1947; *Duval*, 1978]. The abundance of experimental data supporting the model is the reason why we made it our choice. The model adequately describes the nonlinear, transient response both in metals [*Andrade*, 1914] and minerals [e.g., *Jackson*, 1993].

[74] In the time domain, the creep function corresponding to the Andrade model is

$$J(t - t') = J\Theta(t - t') + \beta(t - t')^{\alpha} + \frac{1}{\eta}(t - t'), \qquad (52)$$

η denoting the steady state viscosity, and $J \equiv J(0) = 1/\mu(0) = 1/\mu$ being the unrelaxed compliance, while α and β standing for empirical parameters. Here we employ the Heaviside function $\Theta(t - t')$ to make sure that differentiation of $J(t - t')$, with subsequent multiplication by $\sigma_{\zeta\nu}(t')$ and integration over t', generates the right expression for the strain, with the unrelaxed term $J\sigma_{\zeta\nu}$ present.

[75] Parameter β characterizes the intensity of anelastic friction in the material, and therefore must depend upon the density of the defects. The shape of this dependence remains unknown, because no research has ever been undertaken in this direction in the case of diffusion-driven attenuation. (In this regard, it would be interesting to mention the anelastic-viscoelastic model developed by *Cole* [1995], who managed to express the complex compliance as an explicit function of the defect density in the case of dislocation-driven attenuation.) Experimental measurements [e.g., *Tan et al.*, 2001; *Jackson et al.*, 2002] show that the value of β depends upon the temperature. Theoretical work summarized by *Karato and Spetzler* [1990] also suggests that the attenuation amplitude should be a function of chemistry (e.g., fugacities). Parameter α determines the duration of the transient response in the primary creep. It depends upon the stress and upon the relaxation time of the dominating mechanism of friction [*Castelnau et al.*, 2008]. The values of α for olivine-rich rocks typically fall within the interval 0.1–0.5, most often within 0.2–0.4. A remarkable experimental fact is that the water ice, despite all its physical and chemical differences from minerals, obeys this same law, with the parameter α having values similar to those it has for rocks. This has been indicated by experiments carried out in the grain boundary sliding and in the dislocation creep regimes [*Glen*, 1955; *Jellinek and Brill*, 1956; *Duval*, 1978; *Cole*, 1995; *Castelnau et al.*, 2008].

[76] The Andrade model can be illustrated with a Maxwell element standing in series with an infinite series of dashpots, set in parallel with an infinite series of springs (Figure 1). This configuration reproduces the distribution of relaxation times
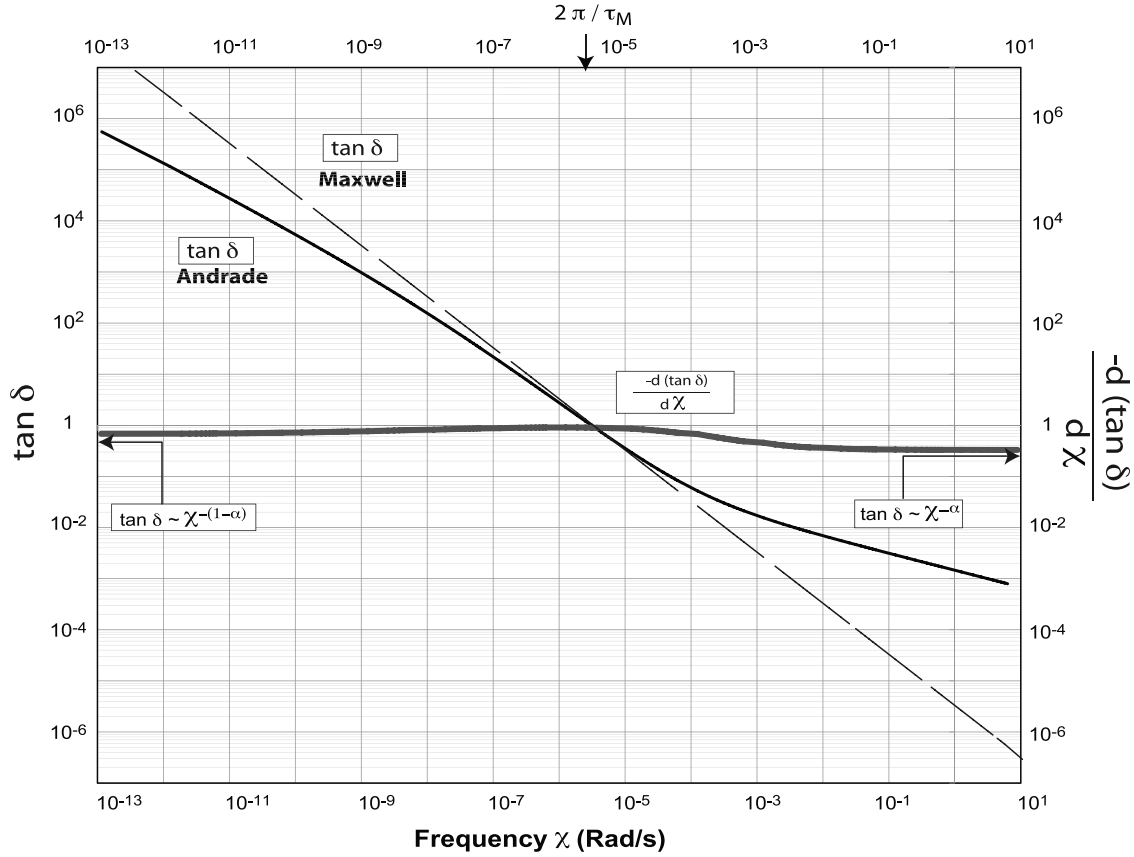
Figure 2. Dissipation spectrum for the Andrade model (thick line) computed from equation (54), with input parameters assuming values relevant to the case of Iapetus: $\alpha = 0.33$, $\beta = 10^{-12}$, $\mu = 3.3$ GPa, and $\eta = 10^{15}$ Pa s. The dashed curve represents the corresponding Maxwell model computed for the same values of unrelaxed shear modulus and viscosity. The thick grey curve represents the slope of the spectrum computed with the Andrade model. The boxes with arrows indicate the trend followed by this slope for infinitely high or infinitely low frequencies.

characterizing the complex transient response of the medium. This peak-broadening construction is inherent also in some other models similar to that of Andrade [e.g., *Cole*, 1995]. As all the other empirical models, the Andrade model is "parametrically economical," though it also shares the main drawback of such models, the "lack of physical transparency" [*Jackson*, 1993]. However, in recent years the transient creep described by the Andrade model was successfully derived via more fundamental approaches describing the motion of defects under stress for different types of defects. grain boundaries in ice [*Castelnau et al.*, 2008], or dislocation jamming in ice [*Miguel et al.*, 2000].

[77] The complex compliance is inferred from the creep function (52) through the Laplace or Fourier transform, provided that the material behaves linearly (which is surely true under weak forcing). According to *Findley et al.* [1976] and *Gribb and Cooper* [1998] the complex compliance for a material obeying the Andrade model is given by

$$\bar{J}(\chi) = J - \frac{i}{\eta\chi} + \beta(i\chi)^{-\alpha}\,\Gamma\,(1+\alpha), \qquad (53)$$

$J = 1/\mu$ being the unrelaxed compliance, χ denoting the frequency, and Γ standing for the Gamma function. Dependence

(53) entails the following expression for the phase lag as a function of the frequency [e.g., *Nimmo*, 2008]:

$$\tan\delta \; = \; -\frac{Im(\bar{J})}{Re(\bar{J})} = \frac{(\eta\chi)^{-1} + \chi^{-\alpha}\,\beta\,\sin\!\left(\frac{\alpha\pi}{2}\right)\Gamma(\alpha+1)}{J + \chi^{-\alpha}\,\beta\,\cos\!\left(\frac{\alpha\pi}{2}\right)\Gamma(\alpha+1)}, \quad (54)$$

whence we see that

$$\begin{aligned}
\tan\delta &\sim \chi^{-\alpha} &&\text{for } \chi \gg \chi_0, \\
\tan\delta &\sim \chi^{(1-\alpha)} &&\text{for } \chi \ll \chi_0.
\end{aligned} \qquad (55)$$

[78] In section 6.3.3, we explain that the parameter β can be expressed in a simple way (63) via J and η. Using that interrelation, it will be easy to demonstrate that the threshold frequency is the inverse Maxwell time:

$$\chi_0 \; = \; \tau_M^{-1} \; = \; \frac{\mu}{\eta} \; = \; (J\,\eta)^{-1}. \qquad (56)$$

[79] The attenuation spectrum derived theoretically from equation (54), with the parameters' values realistic for our study, is presented in Figure 2. Besides the disagreement

between the Andrade and Maxwell model-based curves at high frequencies, which is well documented by laboratory experiments, Figure 2 shows also a difference between the models at very low frequencies. With the insufficient observational data available at low frequencies, it is impossible to say which of the two curves is a better fit over that band. Some scholars favor the Maxwell model, assuming that the mantle is strictly viscous in the low-frequency limit (S. Karato, personal communication, 2010). We shall approach this situation in section 6.4 by bringing in a composite scaling law, which employs the Andrade model to describe the anelasticity of the material in the high-frequency regime and switches to the Maxwell model at low frequencies.

6.3. Mechanisms Driving Internal Friction in Iapetus' Conditions

[80] We open this section with presenting the mechanisms that are likely to drive attenuation in Iapetus (sections 6.3.1–6.3.3). Then we describe how the corresponding physics was implemented in the geophysical model (section 6.3.4). Finally, we illustrate these principles with several numerical runs (section 6.3.5).

6.3.1. Dominating Mechanisms

[81] Ice creep involves several mechanisms whose activations $E*$ energies are close (50–60 kJ mol^{-1} [*Goldsby and Kohlstedt*, 2001]). The creep rate is expressed as a function of the contribution of each mechanism [e.g., *Goldsby and Kohlstedt*, 2001]:

$$\dot{u} = \dot{u}_{BD} + \dot{u}_{VD} + \dot{u}_{DC} + \left(\frac{1}{\dot{u}_{GBS}} + \frac{1}{\dot{u}_{BS}} \right)^{-1} \qquad (57)$$

where BD refers to the boundary diffusion creep (also called Coble creep), VD refers to the grain volume diffusion creep (also called self-lattice diffusion or Nabarro-Herring creep, or self-diffusion, or bulk diffusion), DC refers to the dislocation creep, GBS refers to the grain boundary sliding, and BS refers to the basal slip. The relative contributions from these mechanisms depend on the material grain size (for BD, VD, and GBS) and the magnitude of the stress (for DC, BS and GBS). The stress magnitude determines the amount of mechanical energy available to activate the motion of defects or, in the case of diffusion, to activate breaking of bonds and reorientation of protons.

[82] In Iapetus, the tidal stress is expected to be weak. Being of the order of 10^{-4} MPa, it is at least three orders of magnitude lower than the tidal stress undergone by Enceladus. Accordingly, tidal displacements of Iapetus' surface are about 2 cm, while the strain rate does not exceed 10^{-13} s^{-1}. These values of the tidal displacement and strain are of the same orders of magnitude as the values of the displacement and strain generated by the convective stress [e.g., *Durham and Stern*, 2001]. Accordingly, for low tidal stressing, one should expect dissipation in Iapetus to be dominated by the diffusion creep [*Goodman et al.*, 1981; *Goldsby and Kohlstedt*, 2001; *Barr and Pappalardo*, 2005].

[83] Diffusion creep is known to involve motion of both ionic and orientational (Bjerrum) defects [*Onsager and Runnels*, 1969]. The latter type of defects has been identified as an important source of mechanical and electrical relaxation. Ice is one of the very few materials in which not only translational motion but also rotational motion of defects takes place under stress. Translational is the self-lattice diffusion, i.e., diffusion of material from regions under loading to regions under tension. Rotational is reorientation of the Bjerrum defects (or spin lattice diffusion), which has been much documented due to its notable signature in ice dielectric properties. Another mechanism, the *Coble* [1963] creep, is diffusion of interstitials at the grain boundaries. Being largely responsible for seismic wave attenuation in the Earth's mantle [e.g., *Gribb and Cooper*, 1998], this process is of a lesser importance in cold pure water ice (see below for details). For the stress magnitude and the grain size considered in this study, diffusion may be limited by the basal slip at temperatures below 120 K [*Goldsby and Kohlstedt*, 2001]. At these low temperatures, defect motion is limited (the strain rate is lower than 10^{-29} s^{-1}), so that the contribution of basal slip to the overall dissipation history of Iapetus is negligible.

[84] In the following sections we study the contributions of various types of defect motion in the ice lattice, assuming that Iapetus is made up of a pure water ice, an approximation conventionally used for satellites that contain a small fraction of silicates.

6.3.2. Proton Reorientation

[85] Stress-induced reorientation of water molecules, assisted by the diffusion of orientational (Bjerrum) defects, results in a small anelastic strain whose characteristic relaxation time is strongly dependent on temperature and frequency and is very close to the dielectric relaxation time [*Petrenko and Whitworth*, 1999]. The temperature range, over which proton reorientation is most effective, is defined by the forcing frequency. For the frequencies experienced by Iapetus over its history, this range is from about 150 K down to 125 K. Therefore we have to include proton reorientation in our study, as a mechanism dominating friction at these temperatures.

[86] Proton reorientation is independent of the grain size or stress [*Tatibouet et al.*, 1983]. Although the phase lag measurements by *Tatibouet et al.* [1981, 1983] provide the only available data on proton reorientation at excitation frequencies below 10^{-3} Hz, *Petrenko and Whitworth* [1999] have confirmed the consistency of these results with electric measurements. Besides, the increase in dissipation measured at temperatures from 167 K to 130 K is consistent with the increased mobility of protons [*Johnson and Quickenden*, 1997].

[87] Mechanical measurements indicate that the relaxation peak temperature (the temperature at which the dissipation rate is maximal) decreases with decreasing frequency: from 167 K at 1 Hz to 150 K at 10^{-3} Hz, as reported by *Tatibouet et al.* [1981]. For frequency 10^{-4} Hz and temperature 130 K, these authors obtained tan$\delta = 0.02$. Extrapolating the results linearly to lower temperatures, they suggested that the quality factor could be as low as 40 at the temperature of 125 K and the frequency of 4×10^{-5} Hz (corresponding to tidal excitation of Iapetus with a spin period of 10 h). However, their extrapolation is not consistent with the fact that the proton mobility starts decreasing beginning from 125 K and becomes very limited at 100 K [*Johnson and Quickenden*, 1997], which most probably entails a decrease in dissipation rate. In any case, these measurements indicate that between 100 and 167 K, the quality factor associated with proton
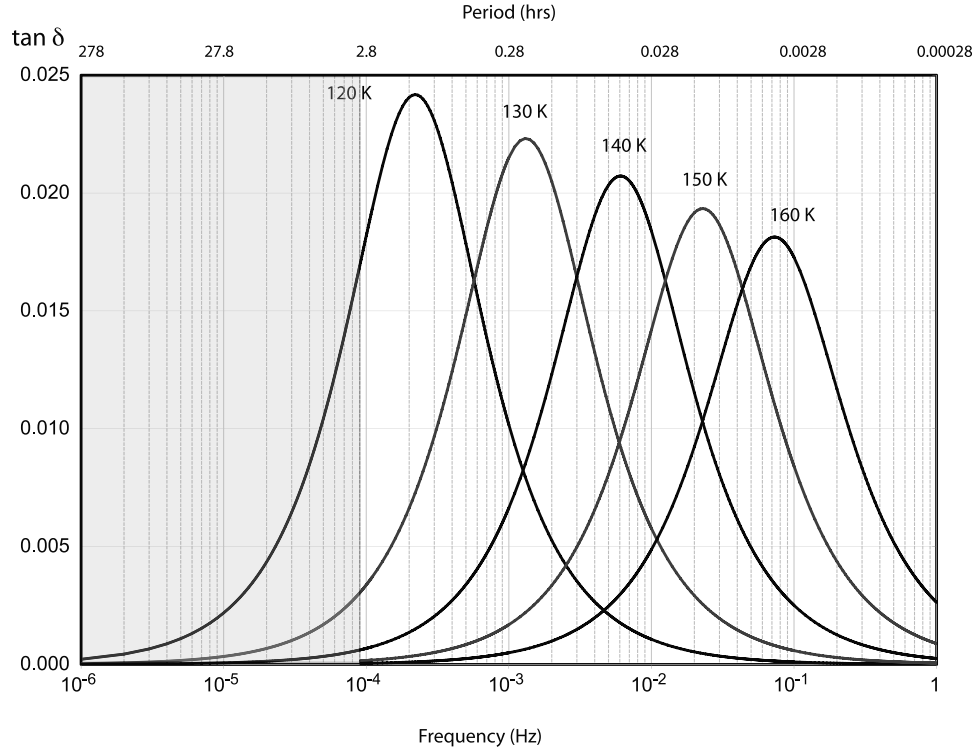
Figure 3. Attenuation resulting from proton reorientation in ice, as a function of the temperature, computed using the parameters from *Tatibouet et al.* [1981]. The temperature of the relaxation peaks is shown as a function of frequency. The calculation is carried out for the temperatures down to 120 K, below which proton mobility gets significantly decreased. For details, see section 6.3.2, specifically formulae (58)–(60).

reorientation is lower than or close to 100. The relaxation time for that mechanism is given by [*Vassoille et al.*, 1974; *Tatibouet et al.*, 1981]:

$$\tau_P = \tau_0 \frac{\exp(E_m/RT)}{c_0 + \exp(-E_f/RT)} \qquad (58)$$

where $E_f(\sim 25 \text{ kJ mol}^{-1})$ and $E_m(\sim 35 \text{ kJ mol}^{-1})$ are the Bjerrum defects' energies of formation and migration, respectively; while c_0 is the concentration of the extrinsic defects that determine the formation of the Bjerrum defects. As suggested by *Tatibouet et al.* [1981], we take $\tau_0 \sim 6 \times 10^{-16}$ s. *Tatibouet et al.* [1981] also demonstrated that the value of c_0 lies between 5×10^{-8} and 10^{-7}. From their experimental measurements, they established an empirical formula for the maximal phase lag (the one at the dissipation peak) as a function of temperature:

$$\tan \delta_{\max} = \frac{E_p}{RT}, \qquad (59)$$

with $E_p \sim 25 \text{ kJ mol}^{-1}$.

[88] Using the available phase lag measurements and taking into account that the friction coefficient has a Debye peak (as has been observed by electric experiments), one can hypothesize that the dissipative behavior dominated by proton reorientation should fit the SAS model because this model permits for a Debye peak. The SAS model connects the stress $\sigma_{\zeta\nu}$ and the strain $u_{\zeta\nu}$ via $\sigma_{\zeta\nu} + \tau_\sigma \dot{\sigma}_{\zeta\nu} = 2\mu(u_{\zeta\nu} + \tau_u \dot{u}_{\zeta\nu})$ with

τ_σ and τ_u being characteristic times, and dot standing for a time derivative. In the frequency domain, this entails: $2\bar{\mu} \equiv \bar{\sigma}_{\zeta\nu}/\bar{u}_{\zeta\nu} = 2\mu \frac{1 + i\tau_u\chi}{1 + i\tau_\sigma\chi}$, wherefrom we obtain: $\tan\delta \equiv \mathcal{I}m[\bar{\mu}]/\mathcal{R}e[\bar{\mu}] = \frac{(\tau_u - \tau_\sigma)\chi}{1 + \tau_u\tau_\sigma\chi^2}$. Thence it is easy to show that the tangent is related to its maximal value through

$$\tan \delta = 2 \, [\tan \delta]_{\max} \frac{\tilde{\tau} \chi}{1 + \tilde{\tau}^2 \chi^2},$$

where the effective relaxation time is defined as $\tilde{\tau} \equiv \sqrt{\tau_\sigma \tau_u}$. It can be identified with the time τ_P given by (58) and can be experimentally determined using the observed shape of the Debye peak. Combining the above equations, we obtain $\tan\delta$ as a function of the temperature and frequency (see Figure 3). Figure 3 shows that proton reorientation is expected to be an important source of dissipation at high forcing frequencies and low temperatures, i.e., at the conditions whereto Iapetus is subject following accretion. As calculated in detail below, this mechanism turns out to be the dominant source of dissipation over the first few hundred million years following the formation of the satellite.

[89] Finally, note that we lack information on the effect of proton reorientation upon the effective elastic modulus. So we assume that the latter remains constant and is equal to the unrelaxed shear modulus $\mu = \mu(0)$.

6.3.3. Diffusion-Assisted Grain Boundary Sliding

[90] Although it is established that diffusion is the dominant mechanism responsible for the Newtonian viscosity of

Table 1. Input Parameters

Parameter	Definition	Value	Source
a	Semimajor axis of the secondary	3,560,820 km	http://ssd.jpl.nasa.gov
A, B, C	Moments of inertia of the satellite ($A < B < C$)	function of evolution	
c_0	Initial concentration in Bjerrum defects	10^{-7}	Tatibouet et al. [1981]
d	Ice grain size	0.1 to 1 mm	
$D_{b,0}$	Preexponential term for the grain boundary diffusion coefficient	6×10^{-4} m^2 s^{-1}	Goldsby and Kohlstedt [2001]
$D_{v,0}$	Preexponential term for the volume diffusion coefficient	9.1×10^{-4} m^2 s^{-1}	Ramseier [1967]
e	Eccentricity of the secondary	0.028 612 5	http://ssd.jpl.nasa.gov
E_b	Activation energy for grain boundary diffusion creep	49 kJ mol^{-1}	Goldsby and Kohlstedt [2001]
E_d	Activation energy for volume diffusion creep	59.4 kJ mol^{-1}	Goldsby and Kohlstedt [2001]
E_f	Activation energy of Bjerrum defect formation	25 kJ mol^{-1}	Tatibouet et al. [1981]
E_m	Activation energy of Bjerrum defect migration	35 kJ mol^{-1}	Tatibouet et al. [1981]
E_p	Activation energy for proton reorientation	25 kJ mol^{-1}	Tatibouet et al. [1981]
g	Surface gravity	0.223 m s^{-2} at the equator	
$M_{s}ec$	Mass of the secondary	1.805 635 $\times 10^{21}$ kg	Jacobson et al. [2006]
n	Mean motion		
R	Satellite's mean radius	735.6 km	Thomas et al. [2007]
T_m	Melting temperature	273 K (268 K if depressed by impurities)	
V_m	Molar volume of defects	1.97×10^{-5} m^3	Fletcher [1970]
w	Grain boundary thickness	9.04×10^{-10} m	Goldsby and Kohlstedt [2001]
α	Input parameters to the Andrade creep equation	0.2 to 0.5	
γ	Newton's gravitational constant	6.674×10^{-11} m^3 kg^{-1} s^{-2}	
$\mu, \mu(0)$	Unrelaxed shear modulus	3.3 GPa	Parameswaran [1987]
τ_0	Reference relaxation time for proton reorientation	6×10^{-16} s	Tatibouet et al. [1981]

ice at low stress [e.g., *Bromer and Kingery*, 1968], it has been little studied experimentally, because this phenomenon is not easily achieved in laboratory conditions [*Duval*, 1978]. Especially, the transient response of ice in the regime of self-diffusion is poorly constrained. The following description is very much inspired by the literature on silicates, with the obvious caveat that experimental measurements are necessary to confirm this approach in application to ices.

[91] The strain rate corresponding to diffusion creep is [after *Goodman et al.*, 1981; *Barr and Pappalardo*, 2005]:

$$\dot{u} = \frac{42 V_m \sigma_{\zeta\nu}}{3 R_G T_m d^2}\left(D_v + \frac{\pi w}{d}D_b\right), \qquad (60)$$

where V_m denotes the molar volume of defects, R is the perfect gas constant, T_m is the melting temperature, d stands for the grain size, w is the grain boundary thickness, while D_v and D_b are the diffusivities of self-diffusion and grain boundary diffusion, respectively. According to *Goldsby and Kohlstedt* [2001], both diffusivities scale with temperature as

$$D_k = D_{k,0} \exp\frac{E_k}{R_G T}, \qquad (61)$$

the subscript $k = v, b$ referring to the volume diffusion and grain boundary diffusion mechanisms, respectively. The parameters $D_{k,0}$ and E_k represent the preexponential magnitude and activation energy of these mechanisms. The values of these parameters are given in Table 1.

[92] In a pure water ice at temperatures well below the premelting regime, the term $\frac{\pi w}{d}D_b$ is several orders of magnitude smaller than D_v, so grain boundary diffusion contributes little to deformation of the material. However, grain boundary diffusion may become significant in the presence of partial melt [*Goldsby and Kohlstedt*, 2001] or impurities [*Bromer and Kingery*, 1968]. We explore these scenarios in section 6.4.

[93] As the temperature dependence of the diffusivity follows the Arrhenius' law, it is possible to rewrite (60) as

$$\dot{u} = \frac{A}{d^2}\exp\left(\frac{-E_v^*}{R_G T}\right), \qquad (62)$$

u signifying the shear strain, E_v^* standing for the activation energy.

[94] *Robuchon et al.* [2010] have suggested that diffusion-creep-driven convection in Iapetus should involve ice grains smaller than 100 μm, as the presence of impurities prevents grain growth. During compaction, grains undergo comminution (size reduction) due to brittle fracture [e.g., *Durham et al.*, 2005]. So we take the said value as an upper bound. We set the lower bound at 1 μm, as observed in the interstellar medium. For the energy of activation, we will use the value by *Ramseier* [1967] of 59.8 kJ mol^{-1}, following the approach of *Goldsby and Kohlstedt* [2001].

6.4. Input to the Andrade Model

[95] The Andrade model (52) contains two dimensionless empirical parameters, α and β. The parameter β quantifies the density and mobility of the defects determining the anelasticity of the material. As seen from (53), the parameter has units s$^{-\alpha}$ Pa^{-1}. Emergence of a parameter with fractional dimensions is an inconvenience, and one should presume that β is a fractional power of a product or ratio of parameters with less exotic dimensions. The experimental literature contains few constraints on the value of β in general. No such data for ices has been published so far. This leaves us no other way but to rely on the data published for silicates. This line of reasoning is legitimate, taken the remarkably universal nature of the Andrade model and its applicability to so many solids. In Figure 4, for each experiment depicted, we have represented β as a function of the viscosity η and shear modulus μ. There, the fits obtained on microcreep data are distinguished from
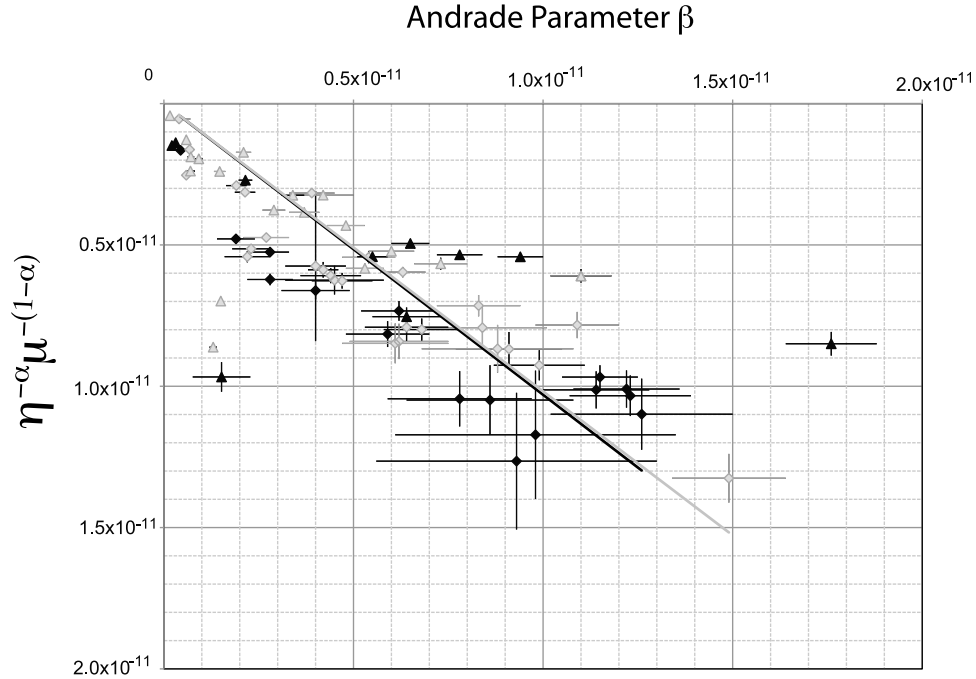
Andrade Parameter β

Figure 4. Attenuation properties of olivine. The Andrade parameter β is depicted as a function of the product $\mu^{-(1-\alpha)}\eta^{-\alpha}$, where α is the Andrade exponential, μ is rigidity, and η is the viscosity. These data are based on spectra inferred from forced oscillation (diamonds) and microcreep (triangles) data obtained by *Tan et al.* [2001] (black) and by *Jackson et al.* [2002] (grey). Fits to the data by a least square method yield the black and grey curves corresponding to the Tan et al. and the Jackson et al. data, respectively. Results are discussed in the text.

those inferred from spectra of forced oscillations. The two methods are complementary, in that the frequency bands of their maximal sensitivity are different. Besides, analysis of microcreep data offer higher resolution when the viscosity decreases. We fitted each series of experiments, using the method of least squares. Overall, the two data sets are consistent with each other. Both are fitted well by a linear curve whose slope is close to 1. Specifically, the slope is ~1.02 for the data set from *Jackson et al.* [2002] and is ~1.03 for the data set from *Tan et al.* [2001]. The R-squared value is 0.62 for the former set but is only 0.39 for the latter set. The difference is largely due to the greater scattering of the microcreep data.

[96] Over the considered range of frequencies, the viscosity decreases by about two orders of magnitude, while the parameter β decreases by one order of magnitude. Despite some scattering in the values of β, we can observe the following relationship between this parameter and the parameters μ and η:

$$\beta \approx \mu^{-1}\,\tau_M^{-\alpha} \;=\; \mu^{-(1-\alpha)}\,\eta^{-\alpha} \;=\; J^{1-\alpha}\,\eta^{-\alpha}, \qquad (63)$$

The interrelation between the viscosity and β is not surprising at all. Both depend on the density of defects and their mobility, and on the appropriate activation energy [e.g., *Webb and Jackson*, 2003]. It should also be recalled that a dependency of the form $(\tau\omega)^\alpha$ with $\alpha \leq 1$ is typical of other models that aim to represent the complex superposition of relaxation

times, such as the extended Burgers element [e.g., *McCarthy and Castillo-Rogez*, 2011] and the model by *Cole* [1995]. We cannot rule out the possibility that that relationship involves an extra factor, which would have been close to one, though.

[97] At this stage, this is the only insight on the quantification of β that appears available. It should certainly be employed with caution outside the range of conditions at which the aforementioned data sets had been acquired (that is for β in the range 10^{-10}–10^{-13} $s^{-\alpha}$ Pa^{-1}). We thus adopt equation (63) as a first-order approximation, keeping in mind that that relationship may have to be updated when a richer volume of laboratory data becomes available. However, for the data at hand, relationship (63) is valid within a factor of two. We would emphasize that relationship (63) is only meant for diffusion-creep-driven anelasticity. It does not necessarily apply to other mechanisms, especially to those involving nonlinear strain.

[98] With (63) taken into consideration, the complex compliance can be expressed through the Maxwell time:

$$\bar{J}(\chi) \;=\; J[1 \;+\; (i\tau_M\chi)^{-\alpha}\,\Gamma\,(1+\alpha)] - \frac{i}{\eta\chi} \qquad (64)$$

In the case of diffusion creep, the Maxwell time $\tau_M = \eta/\mu$ can be inferred from equation (60) as:

$$\tau_M = \frac{3R_G T_m d^2}{42 V_m \mu}\left(D_v + \frac{\pi w}{d}D_b\right)^{-1}, \qquad (65)$$

where we neglect D_b, as the creep is volume diffusion only. Pioneered by *Raj* [1975], expression (65) found its confirmation in experiments on grain boundary diffusion in rocks [*Tan et al.*, 2001; *Jackson et al.*, 2002; *Webb and Jackson*, 2003]. Expressions (63) and (65) indicate that the parameter β is sensitive, mainly through viscosity, to the temperature and the grain size. If the values of the stresses caused by steady state convection and by tide differ by several orders of magnitude (which is believed to be the case of Enceladus and Europa), then different mechanisms may be involved in accommodating these stresses (for example, volume diffusion and grain boundary sliding, respectively). In such a situation, convection and dissipation may still be linked to the material defect geometry (such as grain size), though to a lesser extent, since grain boundary sliding depends on the grain size with an exponent of only 1.4 [*Goldsby and Kohlstedt*, 2001].

[99] For the Andrade parameter α, a range of values between 1/5 and 1/2 has been reported most frequently in the literature on attenuation in ice [*McCarthy and Castillo-Rogez*, 2011].

[100] In the general case of self-diffusion in solids, theoretical study by *Lifshits and Shikin* [1965] suggest that α should be close to 0.5 in the case of grain boundary diffusion. *Jellinek and Brill* [1956], too, report the value of 0.5, though in their paper there is not enough information to confirm that the transient response was indeed driven by the volume diffusion creep. *Lee and Morris* [2010] investigated the microphysical reasons determining the value of α for grain boundary diffusion, and established that α is primarily a function of the presence of impurities at the grain boundaries as well as irregularities in the grain shape. As volume diffusion is also a function of the grain size, we suspect that nonuniform grain geometry plays a role in increasing the value of α. Besides the above references, we have little constraint on the dissipation driven by the volume diffusion. Thus, we explore a wide range of values for α, from 0.2 to 0.5.

[101] The above treatment addressed an anelastic regime, in which diffusion of defects is reversible, so deformation is recoverable. In the viscosity-driven regime, though, diffusion is accompanied by boundary sliding, which is not recoverable. While the attenuation rate in the latter regime is inversely proportional to the viscosity, *Raj and Ashby* [1971] argued that description of this process by the Maxwell model would require some adjustment of the parameters. As their theory was developed for a certain grain geometry, the applicability of their results to icy material remains to be confirmed by further theoretical and experimental research.

6.5. Attenuation Modeling Approach: Summary

[102] Within the combined attenuation model, we take into account proton reorientation, viscosity, and anelasticity of the material. While no interaction between proton reorientation and viscosity or anelasticity has been reported, each mechanism dominates the attenuation response over a specific range of temperatures, so the overlap of the mechanisms at any given time is minimal anyway. Thus, we assume the two mechanisms to act in parallel. To this end, we obtain the overall compliance function by summing up the compliances appropriate to each of the mechanisms involved.

[103] In the case of proton reorientation, we infer the components of the compliance, input to the numerical integration code, through

$$-\frac{\mathcal{I}m[\bar{J}(\chi)]}{\mathcal{R}e[\bar{J}(\chi)]} \;=\; \tan\delta \;=\; 2\,[\tan\delta]_{max}\,\frac{\tau_P\,\chi}{1\,+\,\tau_P^2\,\chi^2}, \qquad (66)$$

The relaxation time τ_P is furnished by equation (58), while $[\tan\delta]_{max}$ is calculated with aid of (59), using parameters presented in Table 1. Most of these being based on the experimental work by *Tatibouet et al.* [1981], we thus have only one data set. As we also lack constraints on the effective modulus of the material in that regime, we assume that $Re(\bar{J}) \sim J$. Further research on this topic is necessary in order to confirm the measurements of *Tatibouet et al.* [1981]. In the case under consideration, the relative contribution from that mechanism to the overall despinning evolution is limited, so that uncertainty in the values of the parameters showing up in (58) bears little implication on the overall results. Still, we included this mechanism for the sake of completeness, in order to highlight a process that could bear greater implications in other contexts.

[104] The combined contribution from the viscous, elastic, and anelastic attenuation is computed within a composite approach, which assumes a Maxwell behavior at frequencies below the threshold defined by (56) and an anelastic-driven regime at higher frequencies, using the Andrade model, and rendered by (53) and (54). However, it should be mentioned that while equation (56) suggests a simple relationship between χ_0 and τ_M, in reality the transitional region from the anelastic regime to the viscosity-dominated regime is complex [*Jackson et al.*, 2002] and may encompass several frequency decades.

[105] The temperature enters equation (54) through the temperature dependence of the viscosity, which is computed with aid of equation (60). The unrelaxed shear modulus μ, too, depends upon the temperature, but this dependence is weak. So we set $\mu = 3.3$ GPa [*Parameswaran*, 1987]. Other relevant parameters are listed in Table 1.

[106] These parameters are established for pure water ice, which is an assumption generally adopted for icy satellites, which, like Iapetus, are dominated by water ice. Still, the presence of soluble (e.g., ammonia) and insoluble (rock) impurities are expected to affect the attenuation behavior of the material.

[107] Their impact depends on their distribution at the grain boundaries (see *McCarthy and Castillo-Rogez* [2011] for a review). Small polar molecules may also be incorporated in the lattice. Dopants, such as ammonia, are generally known to increase dissipation, and to shift the proton-reorientation-caused dissipation peaks toward a lower temperature [e.g., *Petrenko and Whitworth*, 1999; *Oguro*, 2001], but we lack experimental data in conditions relevant to Iapetus, which are needed to properly quantify that effect.

[108] Soluble impurities tend to increase the grain boundary width w and to create regions whose thermodynamic properties depart from those of a pure water ice. As a result, impurities can create a local region whose viscosity is lower than that of the water ice grains. In this case, the assumption that boundary diffusion is not contributing to the material creep, as generally assumed in geophysical modeling does not apply.
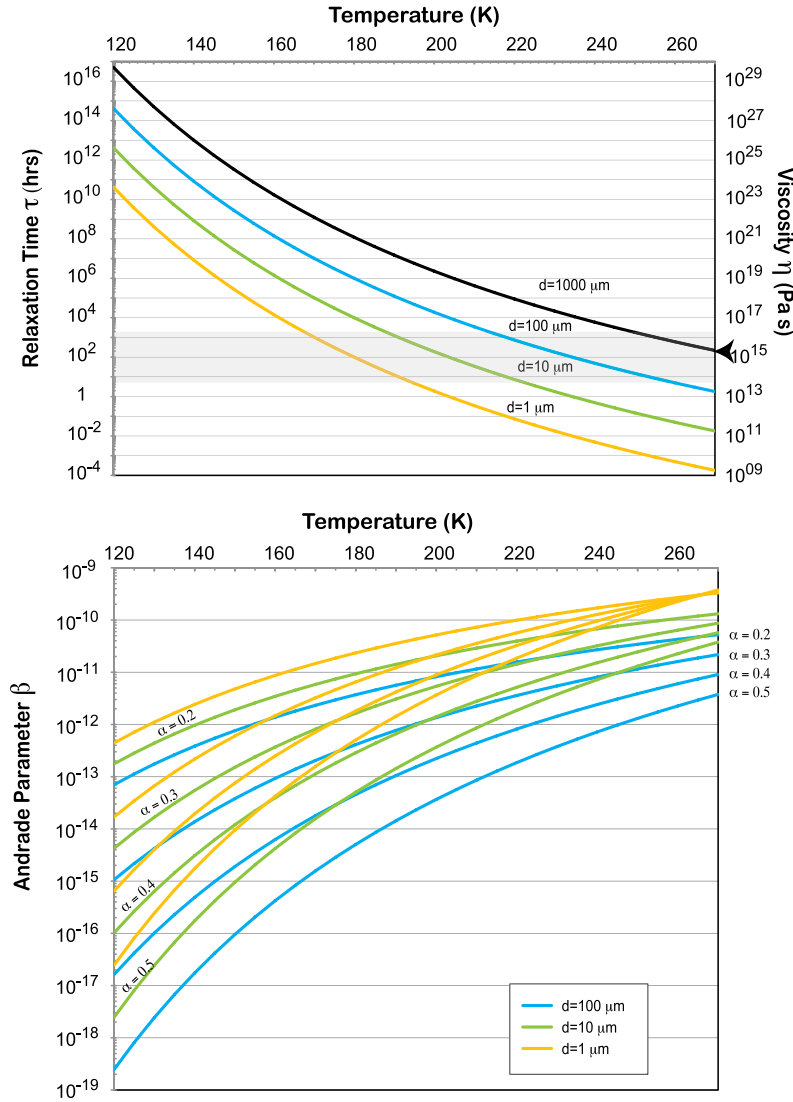
Figure 5. (top) The dependence of the material viscosity and of the relaxation time τ upon the temperature and the grain size d in the case of diffusion creep relevant to this study (see equation (60)). The shaded region corresponds to the realistic range of values assumed by the period of tidal forcing, in the course of Iapetus' despinning. The arrow indicates the approximate viscosity at which the convection onset is expected [*Robuchon et al.*, 2010]. A purely viscoelastic dissipation model implies that at high viscosities the material responds elastically, while at low values of viscosities the viscosity is the dominating factor driving the response. (bottom) The dependence of the parameter β on the temperature, grain size, and α, computed from equation (63). The unrelaxed shear modulus μ is taken as 3.3 GPa [*Parameswaran*, 1987]. (The parameter β has units $s^{-\alpha} Pa^{-1}$.)

[109] Although we currently lack information systematic enough for modeling the impact of soluble impurities on material attenuation at the frequencies relevant to Iapetus' history, we suspect that the effect may play a major role in assisting grain boundary sliding by boundary diffusion or boundary migration. We shall simulate that effect by testing different values for the activation energy of defects at the grain boundaries.

6.6. Numerical Illustration on Simple Models of Iapetus

[110] We present several numerical runs, to illustrate how various processes described in section 6.3 could have contributed to the behavior of a homogeneous water–ice Iapetus.

[111] The dependence of τ_M on temperature, calculated through formulae (65) and (61), is plotted in Figure 5 (top). In the case of Iapetus, the value of τ_M becomes of the same order as the tidal forcing period after formation, when the viscosity becomes greater than $\sim 10^{14}$ Pa s. As pointed out by *Castillo-Rogez et al.* [2007] and *Robuchon et al.* [2010], convection is likely to begin while the material viscosity is at least one order of magnitude greater than the said value, a circumstance which slows down the tidal despinning. However, once the rotation period is of the order of 100 h, a convective Iapetus gets more dissipative and more prone to faster tidal evolution. It then becomes a crucial step to explain how Iapetus' rotation period increased from about 10 h to
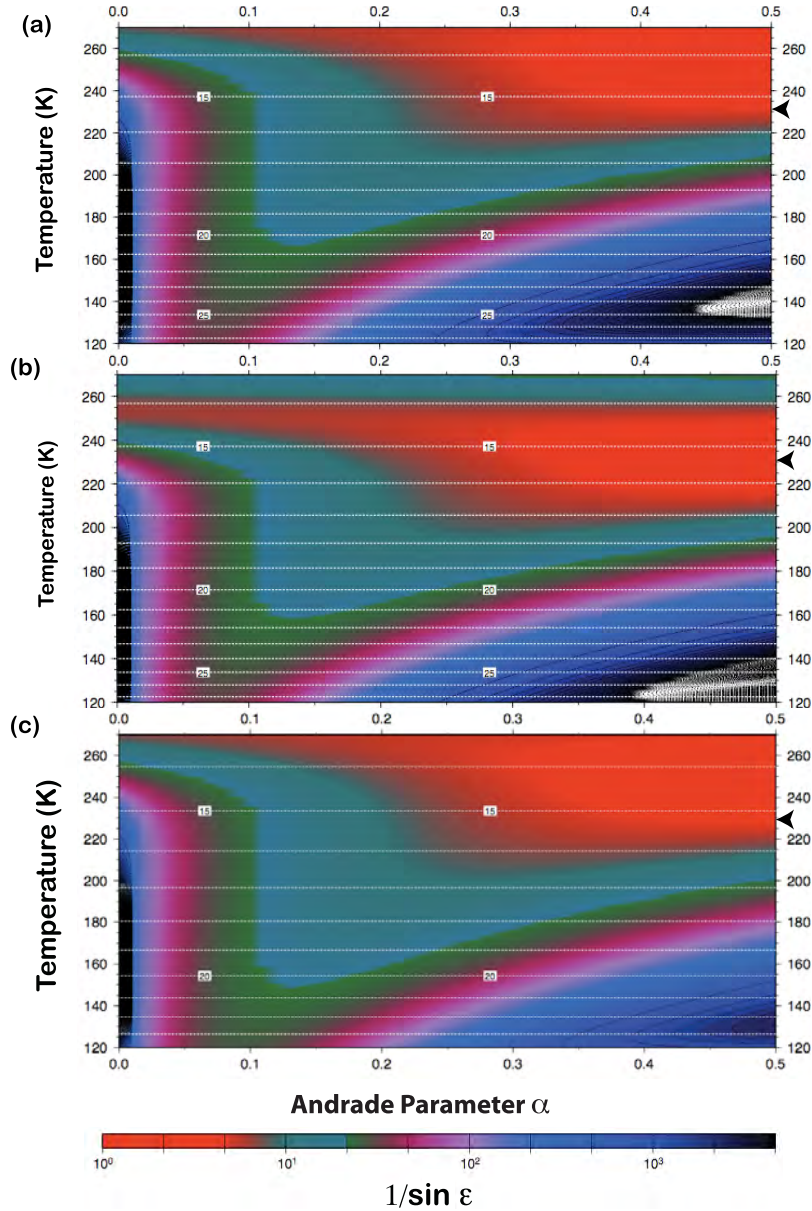
Figure 6. A toy model of dissipation in a "simplified Iapetus" consisting of a pure water ice and having a homogeneous temperature distribution, computed from equation (54). (a) The inverse of $\sin \epsilon$ as a function of the temperature and α, for a grain size of 100 μm and an initial spin period of 10 h. (b) The same as Figure 6a except for an initial spin period of 100 h. White curves indicate the viscosity (in Pa s, logarithm value). (c) The same as Figure 6a except assuming an activation energy for the grain boundary defect diffusion to be 40 kJ mol^{-1}, instead of the value of 49 kJ mol^{-1} accepted by *Goldsby and Kohlstedt* [2001]. The arrows point to a viscosity of 2×10^{15} Pa s at about which convection onset is expected [after *Robuchon et al.*, 2010]. This example reveals the importance of the presence of second-phase volatile impurities decreasing the grain boundary viscosity.

about 100 h, whereafter the tidal dissipation could, in theory, be sufficient to drive despinning to completion.

[112] By (63), we express β as a function of α, which is the other parameter entering the Andrade model (52). In Figure 5 (bottom), we depict the resulting ranges of values, for different temperatures, assuming the material to be a pure water ice. Figure 5 (bottom) tells us that in the case of water ice, β takes values lower than $\sim 10^{-10}$ s$^{-\alpha}$ Pa^{-1}, for the interval of

temperatures that interior of Iapetus is expected to have had over its evolution.

[113] Based on Figure 5 (bottom), we chart the value of $(\sin|\epsilon|)^{-1}$ for Iapetus (using the approach described in section 3.5 and equation (54)), assuming the satellite is homogenous and composed of pure water ice, for a spin period of 10 h and 100 h (Figures 6a and 6b). When α tends toward zero the behavior of the material tends toward a Maxwell body. Taking α equal to zero is equivalent to assuming that the
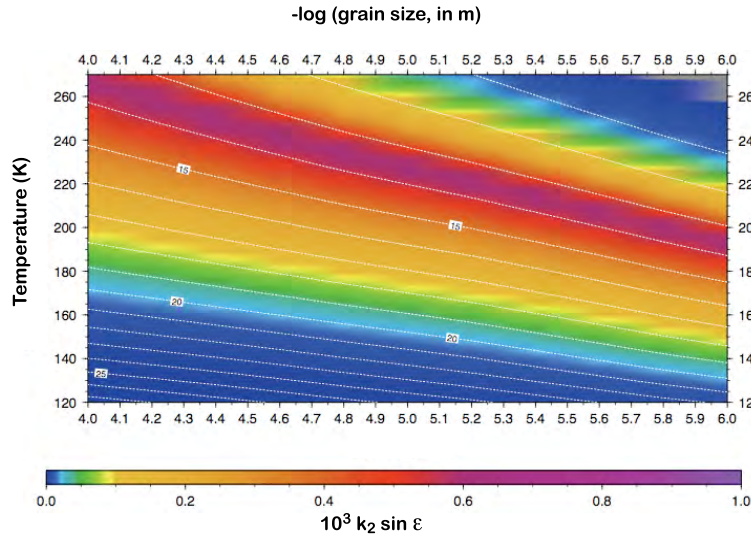
Figure 7. Dissipation in the "simplified Iapetus" consisting of a pure water ice and having a homogeneous temperature distribution. The color background shows the dissipation rate characteristic $k_2 \sin \epsilon$ as a function of the grain size and of the temperature. The contours correspond to the logarithm of the material viscosity, in Pa s. The calculation has been made for a spin period of 10 h and $\alpha = 0.3$. White curves indicate the viscosity (in Pa s, logarithm value). The grey region corresponds to conditions where the model employed in this study becomes unphysical due to the presence of melt.

geometry and distribution of the defects accommodating the tidal stress are uniform in the material, a situation that is obviously not expected in nature. As α increases, the broadening of the relaxation peaks in the material results in increasing the temperature range at which dissipation can be significant. The feature observed in the bottom right corner of Figures 6a and 6b, for temperatures lower than 180 K, is the signature of proton reorientation, which provides a lower bound to $(\sin|\epsilon|)^{-1}$ but is significant only at short periods. On these plots, arrows indicate the regime of temperatures for which convection onset is expected, after *Robuchon et al.* [2010]. The main criterion adopted in this study is that the viscosity becomes smaller than 2×10^{15} Pa s. This implies a bound on the maximal temperature reached in the material. The bound varies as a function of grain size, from 180 K for $d = 10^{-6}$ m to 230 K for $d = 10^{-4}$ m. Within the Maxwell body approach (i.e., for $\beta \to 0$), the temperature has to approach the water-ice melting temperature, for dissipation to be large enough to promote despinning [cf. *Castillo-Rogez et al.*, 2007]. On the other hand, in the present modeling, the value of $1/\sin \epsilon$ can become as small as ~10 at the time of convection onset, especially for values of α greater than 0.2, which may be sufficient to drive despinning.

[114] The dependence of dissipation on the grain size is further illustrated by Figure 7. Figure 7 shows the value of $k_2 \sin \epsilon$ as a function of the grain size and temperature. The product $k_2 \sin \epsilon$ determines the rate of tidal damping. Figure 7 demonstrates that dissipation increases with the decrease of the grain size.

7. Modeling and Results

7.1. Putting Everything Together: The Overall Architecture of the Model

[115] In the current study, we focused on Iapetus' tidal response, while the geophysical part of the model largely repeated the one developed by *Castillo-Rogez et al.* [2007], with some further amendments regarding the parameters of the short-lived radioisotope decay, as suggested by *Castillo-Rogez et al.* [2009]. The latter study suggested a range of times of formation of 3.4 to 5.4 Myr after the production of calcium aluminum inclusions (CAIs), so that heating from [26]Al decay results in compacting most of the interior porosity, a condition sine qua non for preservation of the large departure of Iapetus' shape from hydrostatic equilibrium. In the present study we assumed a time of formation of ~4 Myr after CAIs, leading to a scenario consistent with the current non-hydrostatic shape of Iapetus. Originally, [26]Al came about as a part of the silicate grains that accreted into the planetesimals that later formed icy satellites. The concentration of [26]Al being subject to exponential decay, the time after CAIs defines how much [26]Al is left by the beginning of Iapetus' accretion (which is a fast process believed to have lasted for only about 10^5 years). Thus, the time after CAIs determines the initial concentration of [26]Al considered in the model. For details, see *Castillo-Rogez et al.* [2009].

[116] In our study, we assumed the initial spin period to lie between 7 and 11 h. As demonstrated by *Castillo-Rogez et al.* [2009], Iapetus' semimajor axis did not evolve, over the history of the satellite, by more than a few thousand kilometers. Hence, in the current study we neglected its variations. The moment of inertia C was recomputed at each time step as a function of the appropriate values of the density profile and shape. The necessity to take the evolution of C into account stems from the fact that the equatorial and polar radii could have evolved by more than 15% over the time span between Iapetus' formation and freezing of its shape [*Castillo-Rogez et al.*, 2009].

[117] It would be important to emphasize that the term "fossilization" implies stabilization of the overall geometrical shape of the satellite. Fossilization took place when the spin
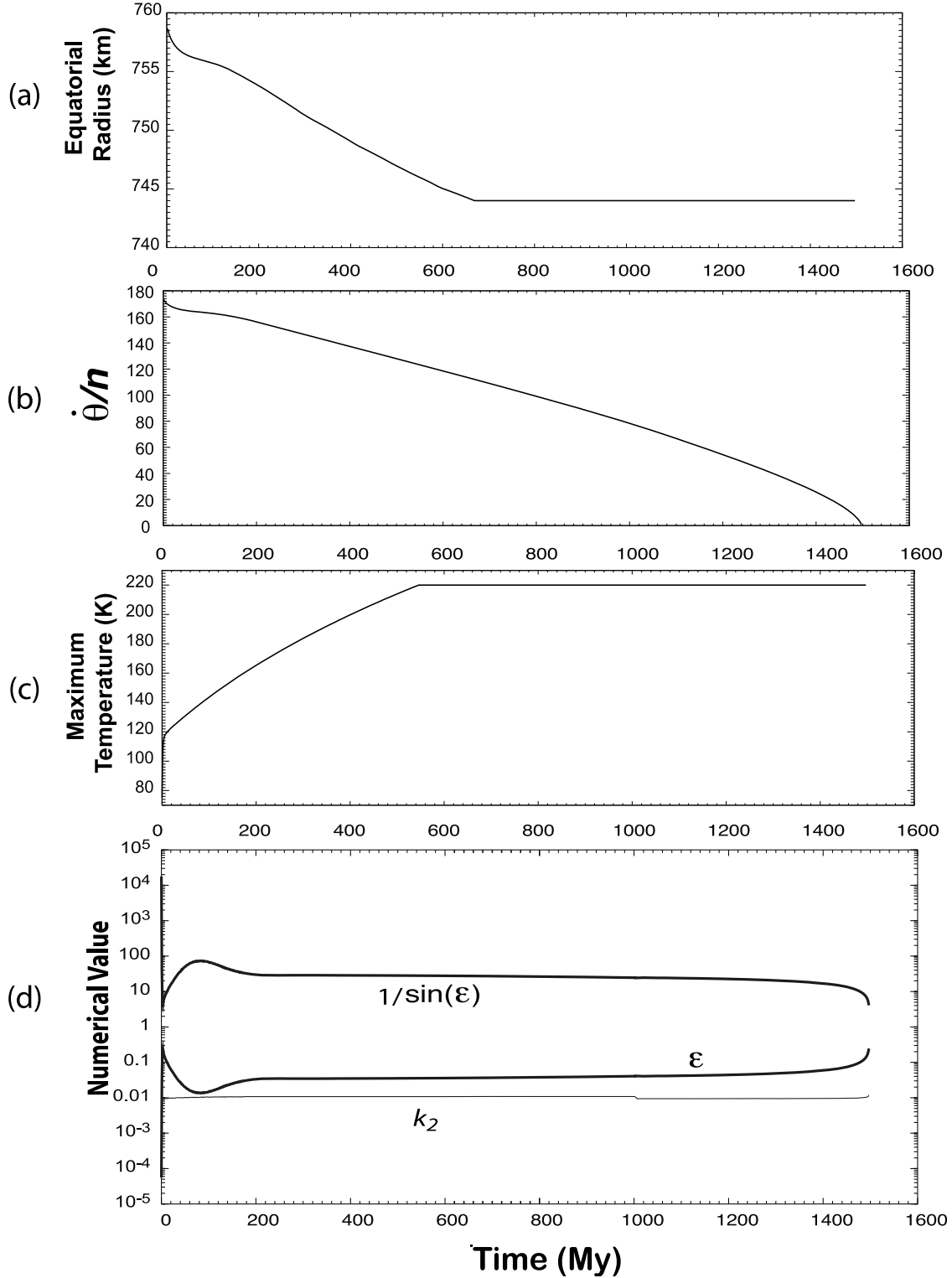
Figure 8. A "typical" scenario of evolution of Iapetus' geophysical and dynamical properties, computed under the following set of assumptions: the time of accretion is 4 Myr after the production of CAIs, the initial spin period is 11 h, the value of the Andrade parameter α is 0.3. The evolution of six parameters is furnished: (d) the tidal phase lag $\epsilon \equiv \epsilon_{2200}$ (corresponding to the principal tidal frequency $\chi \equiv \chi_{2200}$), the inverse sine of the lag, and the Love number k_2; (c) the maximum temperature achieved in the model; (b) the ratio between the spin frequency ω and the mean orbital motion n; and (a) the equatorial radius.
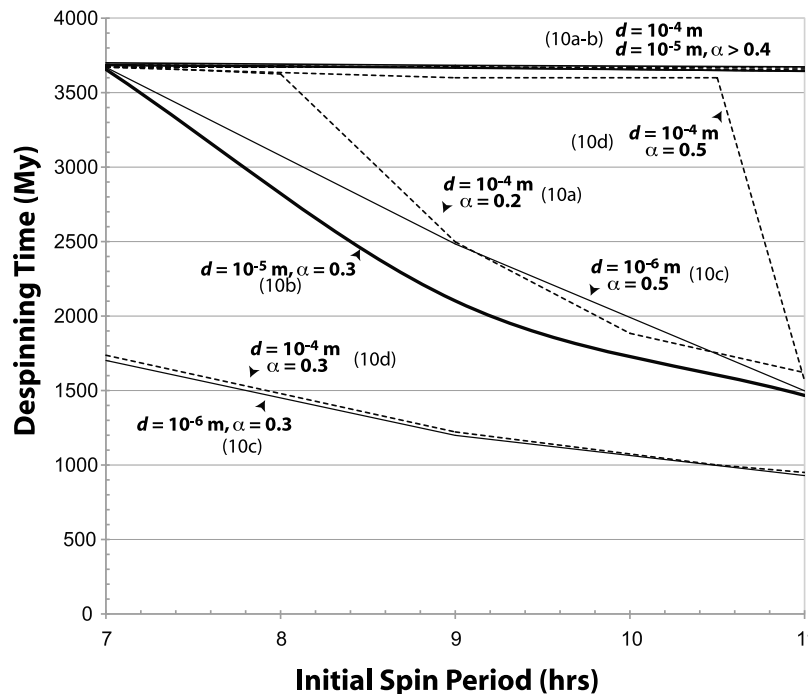
Figure 9. The despinning timescale for Iapetus, as a function of the initial spin period, of the value of the Andrade parameter α, and of various assumptions on material properties. The number and letter in parentheses next to each curve refer to Figures 10a–10d showing the relaxation time of ice for the appropriate case.

period was 15–16 h. This was when the lithosphere became thick enough to support large nonhydrostatic anomalies. This process did not involve freezing of the whole interior. While the thermal properties before and after fossilization were different, fossilization was not a special landmark from the viewpoint of the applicability of our geophysical assumptions. Specifically, the Andrade model was equally applicable before and after fossilization. We in fact assume this model to work since the end of the accretion, when the spin period was 7–11 h. We also assume that the virtual lack of porosity excludes additional dissipation in the brittle regime (cracks, friction between fragments).

[118] From *Castillo-Rogez et al.* [2009], we borrowed a module computing the complex tidal Love number k_2 for multilayered objects, following the method described by *Castillo et al.* [2000] and *Tobie et al.* [2005]. This module yields the time evolution of the following quantities: the material phase lag δ (for each layer), the Love number, the equatorial and polar radii, the moment of inertia, porosity compaction, and the possible differentiation. The knowledge of the rheology for each layer was then used to calculate the overall complex Love number $k_2(\chi)$ for the body as a whole, and to find its dependence upon the tidal frequency χ. In this, as explained in section 3.5, we followed the standard procedure by *Takeuchi and Saito* [1972]. Then the values of $k_2 \sin \epsilon_{2200}(\chi)$, for the current value of the tidal frequency χ, were inserted in formulae from section 4.2 to simulate despinning.

[119] We simulate the consequences of convection by assuming that the viscosity never increases beyond 10^{15} Pa s [*Robuchon et al.*, 2010]. In reality, this constraint is somewhat simplistic, since *Robuchon et al.* [2010] obtained

warmer conditions in some of their models. Thus, our result yields an upper bound on the despinning timescale. In any case, the low dissipation rate resulting from spin evolution is not expected to affect convection (G. Robuchon, personal communication, 2010). We also took into account that the time of convection onset at temperatures greater than 200 K is of the order of several million years [*Robuchon et al.*, 2010].

[120] The parameters used in the model are gathered in Table 1.

7.2. A Typical Scenario

[121] A typical scenario of despinning, in the context of thermal evolution, is presented in Figure 8. Within this example, despinning is achieved over ~1.6 Gyr, while the internal temperature remains lower than 210 K. Over this entire time, the phase lag ϵ obeys $1/\sin|\epsilon| < 100$. Being small after accretion, the parameter $1/\sin|\epsilon| < 100$ increases due to the low temperature. The contribution of proton reorientation at these low temperatures and high forcing frequencies keeps $1/\sin|\epsilon|$ below 100. After a few hundred million years after formation, we get $1/\sin|\epsilon|$ ~30. As the spin period increases, the regime of dissipation evolves from purely anelastic to viscoelastic, and $1/\sin|\epsilon|$ decreases to about 10 and lower, as the spin period becomes greater than 1000 h shortly before the end of despinning (for this particular scenario, at ~1.4 Gyr after formation). An important implication is that despinning evolves gradually, and the phase lag evolution is primarily a consequence of the period evolution. This contrasts with a Maxwell body-based model, in which little despinning occurs until warm temperatures are achieved, and despinning occurs on a very short timescale (i.e., the phase lag evolution is primarily driven by the temperature changes). Thus, the
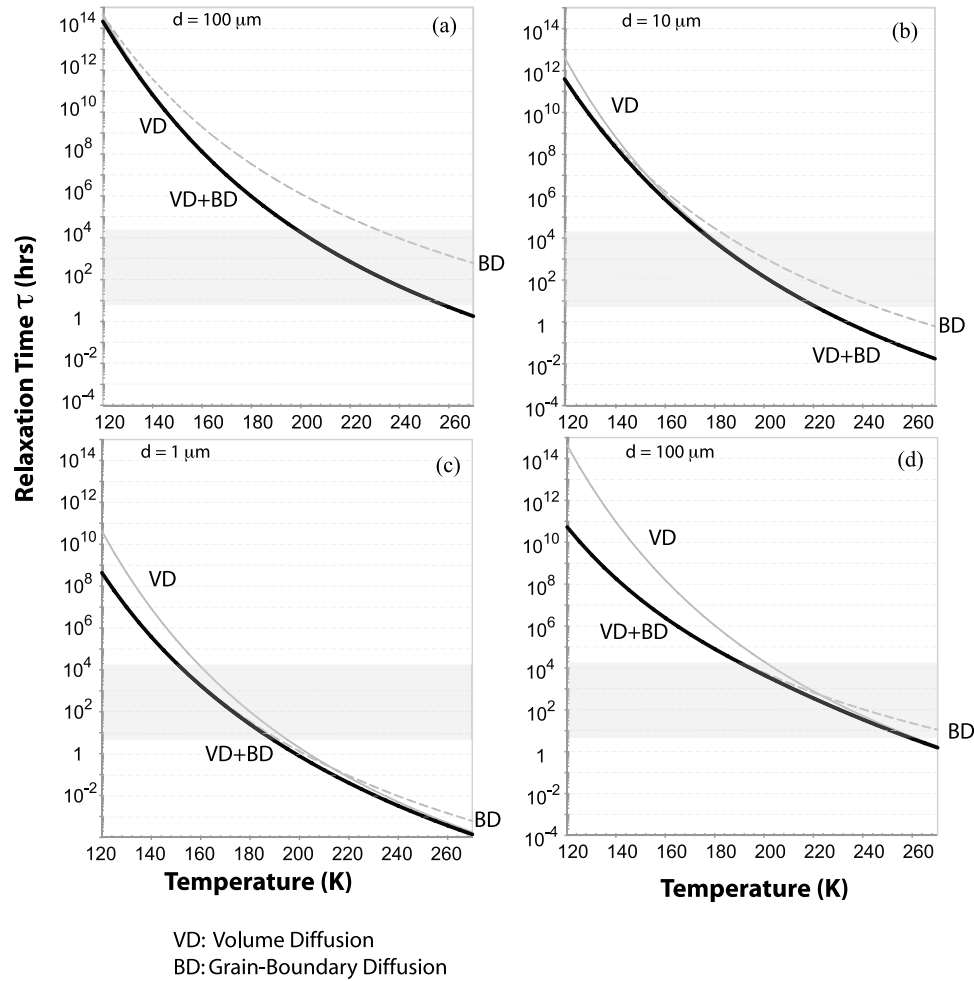
VD: Volume Diffusion
BD: Grain-Boundary Diffusion

Figure 10. Relaxation times for Iapetus' material computed from equation (65), first by considering the volume diffusion (VD) and grain boundary diffusion (BD) separately, and then by summing them (curve labeled VD+BD), after equation (60), and using the input parameters presented in Table 1. The cases in Figures 10a–10c assume pure water ice, with different grain sizes: (a) d = 100 μm; (b) d = 10 μm; and (c) d = 1 μm. (d) Case assumes the presence of a lower activation energy for impurities located at the grain boundaries (E_a = 40 kJ mol^{-1}). The shaded regions correspond to a range of spin periods relevant to this study.

despinning runaway model and rapid shape evolution proposed by *Castillo-Rogez et al.* [2007] are not valid. The latter model suggested a change in the equatorial radius by almost 30% over a few million years. In the current study, the shape evolves as a rate almost constant until its freezing, which takes place at about 600 Myr after formation.

7.3. The Despinning Timescale

[122] The dependencies of the despinning timescale on the key input parameters (the initial spin period, α, and the grain size) are charted in Figure 9. We consider two assumptions about the nature of the ice grain boundaries. Most cases depicted on Figure 9 assume that the activation energy of grain boundary defect migration has the value suggested by *Goldsby and Kohlstedt* [2001], e.g., 49 kJ mol^{-1}. In some situations, though, a lower value of 40 kJ mol^{-1} may be possible, as argued by *Goodman et al.* [1981]. Such a low value may be attributed to the presence of salt impurities. It is

beyond the scope of this study to discuss the validity of the *Goldsby and Kohlstedt* [2001] versus *Goodman et al.* [1981] numbers. The primary goal of these numerical runs is to explore how a simulated departure from the theoretical thermodynamic properties for pure water ice affects the response of the material to mechanical forcing.

[123] In the case of the "theoretical" pure water ice, Figure 9 shows that the despinning time ranges from about 900 to 3700 Myr. The latter is an upper bound reached for a wide range of conditions. Shorter despinning times are possible for a narrow set of conditions, namely for a grain size lower than 10^{-4} m, an initial spin period longer than 10 h, and α smaller than 0.4. It is important to note that if we neglect the grain boundary diffusion creep, and build the attenuation model only using volume diffusion creep, then the despinning time would always be of the order of 3.6 Gyr. This can be understood by considering Figure 10 that shows the relaxation time for grain boundary diffusion and volume diffu-

sion as a function of the temperature and grain size. For $d \geq 0.01$ *mm*, the relaxation time of the material is determined by the volume diffusion for almost the entire relevant temperature range. As the grain size decreases, the grain boundary diffusion mechanism may dominate the global response of the material subject to short-period forcing, leading to a situation where the volume diffusion drives steady state creep, while the grain boundary diffusion dominates at the forcing periods comparable to Iapetus' spin period. If the grain size is of the order of 0.1 mm, the despinning time shows little dependence on the initial spin period and α, and varies by less than 50 Myr over the probed parameter range. Decreasing the grain size to 0.001 mm results in decreasing the despinning timescale by almost a factor 4 if the spin period is 11 h. However, for a spin period lower than 9 h, the despinning timescale is systematically of the order of 3.6 Gyr. In any case, with this approach, we do not find despinning times of a few hundred million years as previously suggested by *Castillo-Rogez et al.* [2007] and *Robuchon et al.* [2010] based on rather arbitrary choices on the input parameters to the attenuation model.

[124] The despinning timescale may be significantly reduced if the effect of impurities is simulated by decreasing the energy of activation and increasing the grain boundary width. If the activation energy is decreased by 15%, as illustrated in Figure 9, the despinning timescale may be less than 1 Gyr. In that case, the dominant mechanism driving defect motion changes from the volume diffusion to the grain boundary diffusion, as the temperature increases (Figure 10). Figure 6c illustrates that for the same conditions as represented in Figure 6a attenuation is increasing over a wider range of temperatures. For example, for a grain size of 10 μm, the maximal attenuation is achieved at a temperature lower by 20 K than that for pure water ice. As a result, attenuation may become geophysically significant for a range of temperature where convection dominates heat transfer, so that convection is not a constraint on despinning duration anymore. Although the choice of parameters for that particular test is arbitrary, it reflects a widespread configuration that associates different mechanisms acting in response to forcing exerted over a broad range of frequencies. This way, shorter despinning times can be made possible by exploring a wider range of parameters characterizing Iapetus' material chemistry.

7.4. Tidal Heating

[125] Within the considered model, most heat is produced deep below the surface. At the temperature about 150 K and a very low porosity, the thermal conductivity of an ice-rock mixture can be as large as 3 W (m K)$^{-1}$ at 150 K. As despinning gets accomplished over a timescale of hundreds of millions of years (at least), we conclude that within the low-porosity model, tidal friction does not contribute considerably to heating of the interior, and thus plays no role in the endogenic activity. (As explained in Appendix A to *Castillo-Rogez et al.* [2007], in the absence of heat transfer, the tidal-stress-generated temperature increase, over hundreds of millions of years, would be about 15 K.)

7.5. The Role of Iapetus' Triaxiality

[126] A spinning satellite is always subject to two torques exerted upon it by its host planet. Besides the aforementioned tidal torque, there exists a torque caused by the satellite's triaxiality. This torque taken into account, expression (44) for despinning rate should be amended to:

$$\ddot{\theta} = -\frac{3}{2} \frac{M_{sec}^2 \gamma k_2 \sin |\epsilon_{2200}|}{\xi \, M_{prim}} \frac{R^3}{a^6} - \frac{3}{2} \frac{B-A}{C} n^2 \frac{a^3}{r^3} \sin 2(\theta - \nu)$$
$$+ \, O(e^2 \sin \epsilon) \, + \, O(i^2 \sin \epsilon), \tag{67}$$

γ standing for Newton's gravitational constant; θ, $\dot{\theta}$, n, and ν denoting Iapetus' sidereal angle, spin rate, mean motion, and true anomaly; while $A \leq B \leq C$ being Iapetus' principal moments of inertia (recomputed at each time step). Through its history, Iapetus' stays mostly homogeneous in density, with no chemical differentiation and almost no porosity; so the evolution of the moments of inertia is defined primarily by the change of shape. After Iapetus gets fossilized, the moments of inertia stay constant.

[127] Since for solid moons and planets their triaxiality typically exceeds the height of the tidal bulge, the triaxiality-caused torque exceeds the tidal torque. Moreover, whenever the orbital eccentricity is not zero, the triaxiality-caused torque has to be taken into account in modeling the approach to the 1:1 spin-orbit resonant state, as was pointed long ago by *Goldreich* [1966]. However, during the despinning stage, the triaxiality-caused torque gets averaged out and therefore plays no major role in the rotational dynamics, until the rotator approaches the final state. This is why, in the first approximation, this torque is often neglected. A more careful study, though, indicates that sometimes the rotational behavior becomes more complicated [*Wisdom et al.*, 1984; *Melnikov and Shevchenko*, 2010], and the triaxiality-caused torque plays an important role in it, especially in the vicinities of the low-order spin-orbit resonances like 5:2, 3:2, etc.

[128] Here we limit ourselves to several numerical runs of equation (67), carried out by means of numerical integrator RA15 authored by *Everhart* [1985]. In our opinion, these runs illustrate the role of the triaxiality-caused term, at least in the context of the chosen dissipation model.

[129] We begin with a more careful investigation of the model considered by *Aleshkina* [2009]. In that model, $k_2 \sin \epsilon_{2200}$ was replaced with k_2/Q, where k_2 was set constant, while Q scaled as the inverse to the tidal frequency. As we already mentioned, this dissipation law is not supported by experimental measurements. The mechanical model with $k_2 = const$ and $Q \propto \chi^{-1}$ can be shortly written down as $k_2/Q \propto \chi$. Branding this model as unphysical, we should keep in mind that the more realistic (Andrade) model (53), too, leads to a similar relation $k_2 \sin \delta_{2200} \propto \chi_{2200}$ between the Love number, the principal tidal frequency χ_{2200}, and the appropriate phase lag δ_{2200}, as demonstrated in Appendix A. The fundamental difference, however, lies in the fact that the unphysical model extends the dependence $k_2/Q \propto \chi$ to the entire range of frequencies χ, including those corresponding to commensurabilities other than 1:1. The realistic model, on its part, simplifies to $k_2 \sin \epsilon_{2200} \propto \chi_{2200}$ only in the closemost vicinity of the 1:1 resonance (where $\chi_{2200} \to 0$), while elsewhere (including the vicinities of the other commensurabilities) it yields, with a good degree of approximation: $k_2 \sin \epsilon_{2200} \propto \chi_{2200}^{-\alpha}$ (for high frequencies) and $k_2 \sin$
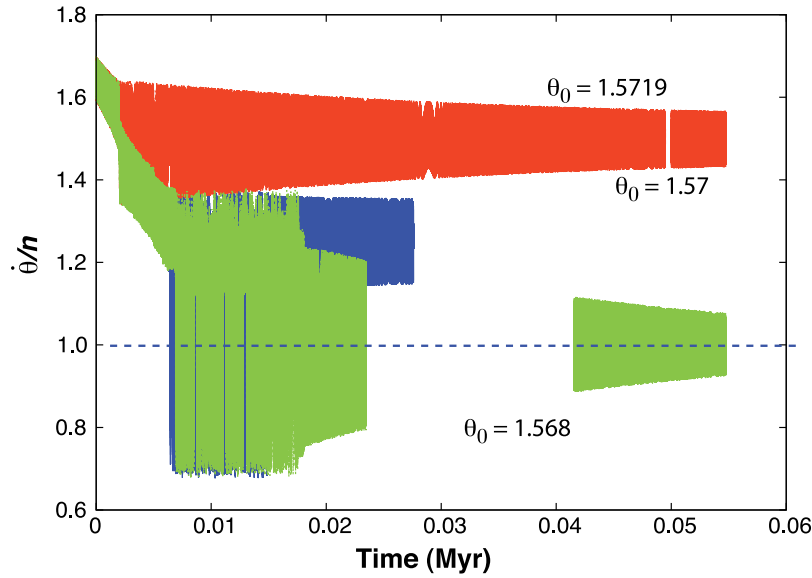
Figure 11. Reexamination of the model employed by *Aleshkina* [2009]. The model includes both the triaxiality-caused torque and the tidal torque (equation (67)) and assumes that the quality factor entering the tidal torque scales as $Q \propto \chi^{-1}$. Here the said model is implemented by three numerical runs, with the same initial condition $\dot{\theta}_0 = 1.7n$ for the spin rate but with slightly different initial conditions for the sidereal angle: $\theta_0 = 1.5680, 1.5700, 1.5719$ rad.

$\epsilon_{2200} \propto \chi_{2200}^{-(1-\alpha)}$ (for low frequencies), both α and $(1 - \alpha)$ being positive.

[130] The second aspect of Aleshkina's model, which we intend to reexplore, is the role of triaxiality at various initial conditions. Individual evolutionary paths, which differ through tiny changes in initial conditions, are all equally valid statistical representatives of the actual system. So we reexamined Aleshkina's results by performing three simulations with slightly distinct initial values of the sidereal angle: $\theta_0 = 1.5680, 1.5700, 1.5719$ radian. To simplify the comparison of
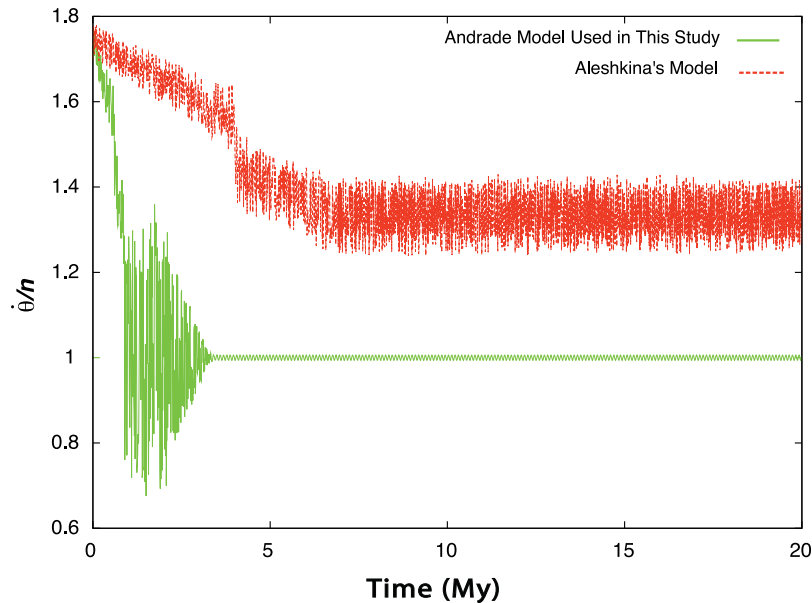

Figure 12. Comparison of two scenarios of Iapetus' tidal despinning. One scenario is based on the Andrade dissipation model explored in this paper; another is based on the model $Q \propto \chi^{-1}$ employed by *Aleshkina* [2009]. In both cases, the triaxiality-generated torque was included. This torque did not cause major changes to the scenario based on the Andrade model. However, it brought a temporary entrapment (in the 3:4 resonance) into the scenario based on the model $Q \propto \chi^{-1}$. This happened because the latter model implies an unrealistic increase of the Q factor at low frequencies, leading to an unrealistic decrease of the despinning rate and, as a result, to a higher probability of temporary entrapments in intermediate resonances.

the thus obtained results with those reported by *Aleshkina* [2009], we began all three simulations with the same initial spin rate $\dot{\theta}_0 = 1.7n$, and used for all the involved parameters the same values as *Aleshkina* [2009]. To decrease the simulation time, we multiplied the tidal torque by a factor of one thousand. This method is often employed to study the behavior of dynamical systems. It is legitimate as long as the timescales of dissipative mechanisms much exceed those of nondissipative forces. As the tidal torque is dissipative and acts on very long timescales, we artificially accelerate its action. On the other hand, the triaxiality-caused torque is left untouched, since we do not want to change the physics on the short timescale.

[131] Figure 11 shows the three resulting scenarios of Iapetus' despinning, within Aleshkina's model implemented under three slightly different initial conditions imposed on θ. The first choice of the initial condition, $\theta_0 = 1.5680$ rad, leads to Iapetus' crossing the low-order spin-orbit resonances, with no obvious time delay. The other two choices, $\theta_0 = 1.5700$ rad and $\theta_0 = 1.5719$ rad, result in Iapetus getting stuck for a significant amount of time in both the 5:4 and 3:2 resonances. While the friction law $Q \propto \chi^{-1}$ employed by *Aleshkina* [2009] guarantees exceedingly long tidal-despinning times, there may be a possibility that the afore described delays in low-order resonances led to further elongation of those times of *Aleshkina* [2009].

[132] To emphasize the role that the frequency dependence of dissipation plays in the tidal-despinning process, in Figure 12 we compare two scenarios based on different dissipation models. One scenario is based on the observation-based dissipation model explored in the present work, another on the model $Q \propto \chi^{-1}$ employed by *Aleshkina* [2009]. Since in the observation-based model the quality factor does not increase rapidly at low frequencies, this model keeps despinning fast even when the ratio $\dot{\theta}/n$ becomes of order unity. However, in the $Q \propto \chi^{-1}$ model the quality factor grows at low frequencies, thus providing much lower despinning rate, and increasing the chances for getting temporarily stuck at the intermediate resonances due to the triaxiality-generated torque; see the long-term entrapment in the 4:3 resonance in Figure 12.

8. Conclusions

[133] We have examined the despinning history of Iapetus, using the mechanical model of Andrade which is quite different from models employed in the literature hitherto. Our approach is based on the observation that under the stress and temperature conditions relevant to Iapetus following accretion, the most likely anelastic and viscoelastic dissipation mechanisms involve the motion and rearrangement of defects in the ice lattice (self-lattice diffusion). In this sense, Iapetus is typical, in that most of the other large icy moons, too, are subject to low tidal stressing. (Internal friction in satellites subject to high tidal stress, such as Europa, Enceladus, Miranda, Ariel, is likely to be dominated by dislocations or grain boundary sliding as primary drivers of dissipation [e.g., *McCarthy and Castillo-Rogez*, 2011, Figure 1].)

[134] Our study is based on the Andrade model, which has proven adequate to describe anelasticity in a wide variety of materials, including ices. An important improvement of this

approach upon earlier models is that it has enabled us to combine the viscous and transient creep components within one model, in a self-consistent manner. We also explored the role of proton reorientation as an additional source of attenuation leading to a possible departure of the dissipation law from the Andrade model at certain temperatures. Using the available empirical data as well as necessary extrapolations, we have demonstrated that tidal dissipation in Iapetus is sufficient to achieve efficient despinning at temperatures much below the water ice melting temperature. Under these conditions, the effect of convection as a factor limiting dissipation and despinning, pointed out by *Castillo-Rogez et al.* [2007] and explored by *Robuchon et al.* [2010], is no longer an obstacle.

[135] At the same time, our study has highlighted certain difficulties inherent in this type of problems. Specifically, if we model dissipation under the assumption that Iapetus consists of a pure water ice, the resulting despinning timescales come up to about 4 Gyr, a result that may be inconsistent with the available geological data. Then impurities, whose presence in the ice-dominated satellites is suspected but whose affect is generally not quantified, may have a significant impact on the attenuation mechanism. Rock impurities are expected to inhibit boundary sliding at these stress levels [*Raj*, 1975], while low-eutectic, second-phase volatiles are likely to decrease the viscosity locally by promoting defect mobility. While the prospect of investigating these processes in future is most appealing, virtually no experimental data are available so far. This has limited our ability to narrow down our estimates for Iapetus' despinning timescale. While the obtained estimate places the despinning time within the interval from 0.9 Gyr through 3.7 Gyr, a more exact estimate will remain unavailable until we learn more about the influence of impurities upon dissipation in ices. (While the experimental literature offers some data on dissipation in dirty ices, those data are typically obtained under forcing several orders of magnitude higher than the tidal stress expected in most icy satellites. Hence the applicability of such data in our study remains questionable.)

[136] We have also pointed out that by adding the triaxiality-caused torque to the tidal one, we encounter a chaotic behavior at the final stage of despinning, a behavior that sometimes includes long-term entrapments in the intermediate resonances. Although this phenomenon needs further investigation, our numerical runs indicate that entrapment becomes more likely when one employs the unphysical model $Q \propto \chi^{-1}$ in calculation of the tidal torque. Such a model entails an unrealistic increase of the Q factor at low frequencies, leading to an unrealistic decrease of the despinning rate and, as a result, to a higher probability of temporary entrapments in intermediate resonances. On the other hand, when calculation of the tidal torque is based on a more realistic mechanical model, the tidal torque remains large enough even at the latest stages of despinning. So the despinning rate stays sufficiently high, thus reducing the chances of getting stuck at an intermediate resonance.

[137] Finally, in Appendix A, we explained why the dissipation models $Q \sim \chi^{\alpha}$, with a positive α, do not lead to infinities in the expressions for the tidal torque or force. (Incorrect claims of existence of such infinities appeared in the literature more than once.) Although *Efroimsky and*

Williams [2009] already addressed this point, here we explained it more carefully.

Appendix A: Behavior of $|k_2(\chi)| \sin \epsilon_2(\chi) = -\mathcal{I}m\,[\bar{k}(\chi)]$ in Various Frequency Bands, for the Andrade and Maxwell Models

[138] *Efroimsky and Williams* [2009] emphasized that the empirical model $Q \sim \chi^\alpha$ with a positive α does not doom the *lmpq* term of the torque to explode on arrival at the *lmpq* resonance. While the frequency χ_{lmpq} approaches zero, it should be remembered that the said tidal term actually contains not k_l/Q but $k_l \sin \epsilon_l$, the phase lag being related to the quality factor via (6) or (7), dependent on how exactly the quality factor is defined.

[139] *Efroimsky and Williams* [2009] mentioned that in the limit of vanishing frequency, the Love number scales in the leading order as

$$k_2(\chi) \approx k_2(0) \cos \epsilon_2(\chi). \qquad (A1)$$

However, our justification of (A1) was less than solid. We referred to a very empirical hydrodynamical treatment by *Alexander* [1973]. We also mentioned, with no proof, that by using formulae from *Churkin* [1998] it is possible to prove (A1) for a broad class of models.

[140] Here we shall demonstrate that (A1) works well for the Maxwell model. For the Andrade body, though, it gets replaced with a more complicated expression. Nonetheless, as proven below, crossing of a resonance portends no difficulties, because the crucial factor $k_l \sin \epsilon_l$ vanishes smoothly as the moon gets into a resonance.

[141] Generally, $|\bar{k}_l(\chi)| \sin \epsilon_l(\chi) = -\mathcal{I}m[\bar{k}_l(\chi)]$. It is straightforward from (27) that

$$
\begin{aligned}
\bar{k}_l(\chi) &= \frac{3}{2(l-1)} \frac{\bar{J}(\chi)}{\bar{J}(\chi) + A_l J} \\
&= \frac{3}{2(l-1)} \frac{\mathcal{R}e[\bar{J}(\chi)] + i\mathcal{I}m[\bar{J}(\chi)]}{\mathcal{R}e[\bar{J}(\chi)] + A_l J + i\mathcal{I}m[\bar{J}(\chi)]}
\end{aligned} \qquad (A2a)
$$

so that

$$
\bar{k}_l(\chi) = \frac{3}{2(l-1)}
$$
$$
\cdot \frac{(\mathcal{R}e[\bar{J}(\chi)])^2 + (\mathcal{I}m[\bar{J}(\chi)])^2 + A_l J \mathcal{R}e[\bar{J}(\chi)] + iA_l J \mathcal{I}m[\bar{J}(\chi)]}{(\mathcal{R}e[\bar{J}(\chi)] + A_l J)^2 + (\mathcal{I}m[\bar{J}(\chi)])^2},
$$
$$(A2b)$$

wherefrom

$$
\begin{aligned}
|\bar{k}_l(\chi)| \sin \epsilon_l(\chi) &= -\mathcal{I}m[\bar{k}_l(\chi)] = \frac{3}{2(l-1)} \\
&\cdot \frac{-A_l J \mathcal{I}m[\bar{J}(\chi)]}{(\mathcal{R}e[\bar{J}(\chi)] + A_l J)^2 + (\mathcal{I}m[\bar{J}(\chi)])^2},
\end{aligned} \qquad (A3)
$$

where $J = J(0) = 1/\mu = 1/\mu(0)$ may be chosen as the unrelaxed compliance (see the paragraph after formula (26)). For an Andrade body, the complex compliance $\bar{J}$ is given by (53). Its imaginary and real parts are

$$\mathcal{I}m[\bar{J}(\chi)] = -\frac{1}{\eta \chi} - \chi^{-\alpha} \beta \sin\left(\frac{\alpha\pi}{2}\right)\Gamma(\alpha + 1), \qquad (A4)$$

$$\mathcal{R}e[\bar{J}(\chi)] = J + \chi^{-\alpha} \beta \cos\left(\frac{\alpha\pi}{2}\right)\Gamma(\alpha + 1) \qquad (A5)$$

Introducing the Maxwell time

$$\tau_M \equiv \frac{\eta}{\mu} = \eta J, \qquad (A6)$$

and recalling that $A_l \gg 1$, we can easily derive from (63) and (A4)–(A5) that

$$|\bar{k}_l(\chi)| \sin \epsilon_l(\chi) \approx \frac{3}{2(l-1)} \frac{1}{A_l} \sin\left(\frac{\alpha\pi}{2}\right)\Gamma(\alpha + 1)(\tau_M \chi)^{-\alpha}$$
$$\text{for} \quad \chi \gg \tau_M^{-1}, \qquad (A7)$$

$$|\bar{k}_l(\chi)| \sin \epsilon_l(\chi) \approx \frac{3}{2(l-1)} \frac{1}{A_l} (\tau_M \chi)^{-1}$$
$$\text{for} \quad \tau_M^{-1} \gg \chi \gg \tau_M^{-1} A_l^{-1}, \qquad (A8)$$

$$|\bar{k}_l(\chi)| \sin \epsilon_l(\chi) \approx \frac{3}{2(l-1)} A_l \tau_M \chi \quad \text{for} \quad \tau_M^{-1} A_l^{-1} \gg \chi. \quad (A9)$$

Expressions (A7) and (A8) coincide with the frequency dependencies of $|\bar{J}(\chi)| \sin \delta(\chi) = -\mathcal{I}m[\bar{J}(\chi)]$ in the high- and low-frequency bands, as can be demonstrated from (53). However, (A9) renders a feature characteristic of the tidal lagging, and not of that in the material. We owe this feature to self-gravitation, i.e., to the presence of the first term in the denominator of formula (25).

[142] For realistic values of the parameters of icy satellites (say, $\mu \sim 10^9$ *Pa*, $\eta \sim 10^{11}$ Pa s, and $A_l \sim 10^3$), the condition $\tau_M^{-1} A_l^{-1} \gg \chi$ puts χ below 10^{-5} Hz. This indicates that $|\bar{k}_l(\chi)| \sin \epsilon_l(\chi)$ behaves as (A9) only in an extremely close vicinity of the resonance corresponding to vanishing of the mode χ. Still, it is important that the quantity $|\bar{k}_l(\chi)| \sin \epsilon_l(\chi)$ grows to a finite maximum and then vanishes rapidly but smoothly, as the frequency falls to zero. So the expression for the tidal torque or tidal force experiences no infinities when the moon approaches a resonance.

[143] As mentioned in section 3.3, in reality the potential $\bar{U}$ and therefore also $\bar{k}$ are functions not of the positively defined frequencies χ but of the tidal modes ω which can be positive or negative. Employing χ instead of ω, we must compensate for this abuse by multiplying the lag $\epsilon_l(\chi_{lmpq})$, "by hand", with $\text{sgn}\,\omega_{lmpq}$. This way, in actual computations each expression (A7)–(A9) must be amended with this factor. Then, for example, (A9) will read as $|\bar{k}_l(\chi_{lmpq})| \sin \epsilon_l(\chi_{lmpq}) \approx \frac{3}{2(l-1)} A_l \tau_M \chi_{lmpq}\, \text{sgn}\,\omega_{lmpq} = \frac{3}{2(l-1)} A_l \tau_M \omega_{lmpq}$. From this we see that most naturally, the *lmpq* term of the torque changes its sign on crossing the *lmpq* resonance.

[144] Finally, we would point out that the general expression (A2a) furnishes the expression for $|\bar{k}_l(\chi)|$, while (A4) and (A5) render the expression for $\tan \epsilon_l(\chi) = -\mathcal{I}m[\bar{k}_l(\chi)]/\mathcal{R}e\,\mathcal{R}e[\bar{k}_l(\chi)]$. From these expressions, it is easy to demonstrate

that (A1) indeed works, for the Maxwell model, in the low-frequency limit. However, for the Andrade model the relation between $|\bar{k}_l(\chi)|$ and $|\bar{k}_l(0)|$ becomes more complicated. Interestingly, for the Kelvin-Voigt model relation (A1) is exact at all frequencies.

Notation

a semimajor axis.
A, B, C moments of inertia of the satellite ($A < B < C$).
c_0 initial concentration in Bjerrum defects at a reference temperature.
d ice grain size.
D_b diffusivity of grain boundary diffusion.
D_v diffusivity of volume diffusion.
e eccentricity of the secondary.
E tidal energy.
E_a activation energy for diffusion creep.
E_f activation energy of Bjerrum defect formation.
E_m activation energy of Bjerrum defect migration.
$F_{lmp}(i)$ inclination functions.
g surface gravity.
$G_{lpq}(e)$ eccentricity polynomials.
i inclination of the secondary.
l degree (spherical harmonics).
$J, J(0)$ compliance.
k_l tidal Love number of degree l.
M_{prim} mass of the primary (satellite).
M_{sec} mass of the secondary (planet).
$\mathcal{M}$ mean anomaly.
n mean motion.
p slope of the attenuation spectrum.
P_l Legendre polynomial of degree l.
Q dissipation factor.
r radius.
R satellite's mean radius.
R_G gas constant.
t time.
T temperature.
T_m melting temperature.
u shear strain.
V_m molar volume of defects.
w grain boundary thickness.
W stationary tidal change of the potential.
α, β input parameters to the Andrade creep equation.
χ physical frequencies of deformation.
δ material phase lag.
Δt time lag.
ΔE energy loss.
Δ dissipation strength.
ϵ tidal phase lag.
η steady state viscosity.
γ Newton's gravitational constant.
λ longitude.
Γ gamma function.
$\mu, \mu(0)$ unrelaxed shear modulus.
υ true anomaly.
ω argument of the pericenter.
Ω longitude of the node.
φ initial phase.
ϕ latitude.
σ shear stress.
τ_M Maxwell time.
τ_V Voigt time.
τ_P relaxation time for the proton reorientation mechanism.
$\mathcal{T}$ tidal torque.
Θ Heaviside function.
θ sidereal angle.
$\dot{\theta}$ spin rate.
ξ dimensionless mean moment of inertia.
ζ, ν tensor indices.

References

Aleshkina, E. Y. (2009), Synchronous spin-orbital resonance locking of large planetary satellites, *Sol. Syst. Res.*, *43*, 71–78, doi:10.1134/S0038094609010079.

Alexander, M. E. (1973), The weak-friction approximation and tidal evolution in close binary systems, *Astrophys. Space Sci.*, *23*, 459–510, doi:10.1007/BF00645172.

Andrade, E. N. da C. (1910), The viscous flow in metals, and allied phenomena, *Proc. R. Soc. London, Ser. A*, *84*, 1–12, doi:10.1098/rspa.1910.0050.

Andrade, E. N. da C. (1914), The flow in metals under large constant stresses, *Proc. R. Soc. London, Ser. A*, *90*, 329–342, doi:10.1098/rspa.1914.0056.

Barr, A. C., and R. T. Pappalardo (2005), Onset of convection in the icy Galilean satellites: Influence of rheology, *J. Geophys. Res.*, *110*, E12005, doi:10.1029/2004JE002371.

Brill, R., and P. R. Camp (1961), Properties of ice, *Res. Rep. 68*, SIPRE Snow, Ice, and Permafrost Res. Estab., U.S. Army Terr. Sci. Cent., Hanover, N. H.

Bromer, J. D., and W. D. Kingery (1968), Flow of polycrystalline ice at low stresses and small strains, *J. Appl. Phys.*, *39*, 1688–1691, doi:10.1063/1.1656416.

Castelnau, O., P. Duval, M. Montagnat, and R. Brenner (2008), Elastoviscoplastic micromechanical modeling of the transient creep of ice, *J. Geophys. Res.*, *113*, B11203, doi:10.1029/2008JB005751.

Castillo, J. C., A. Mocquet, and C. Sotin (2000), Détecter la présence d'un océan dans Europe à partir de mesures altimétriques et gravimétriques, *C. R. Acad. Sci., Ser. 2, Sci. Terre Planetes*, *330*, 659–666, doi:10.1016/S1251-8050(00)00195-6.

Castillo-Rogez, J. C., D. L. Matson, C. Sotin, T. V. Johnson, J. I. Lunine, and P. C. Thomas (2007), Iapetus' geophysics: Rotation rate, shape, and equatorial ridge, *Icarus*, *190*, 179–202, doi:10.1016/j.icarus.2007.02.018.

Castillo-Rogez, J. C., T. V. Johnson, M. H. Lee, N. J. Turner, D. L. Matson, and J. I. Lunine (2009), ^{26}Al decay: Heat production and a revised age for Iapetus, *Icarus*, *204*, 658–662, doi:10.1016/j.icarus.2009.07.025.

Churkin, V. A. (1998), The Love numbers for the models of inelastic Earth (in Russian), Preprint 121, Inst. of Appl. Astron., St. Petersburg, Russia.

Coble, R. K. (1963), A model for boundary diffusion controlled creep in polycrystalline materials, *J. Appl. Phys.*, *34*, 1679–1682, doi:10.1063/1.1702656.

Cole, D. M. (1990), Reversed direct-stress testing of ice: Initial experimental results and analysis, *Cold Reg. Sci. Technol.*, *18*, 303–321, doi:10.1016/0165-232X(90)90027-T.

Cole, D. M. (1995), A model for the anelastic straining of saline ice subjected to cyclic loading, *Philos. Mag. A*, *72*, 231–248, doi:10.1080/01418619508239592.

Cooper, R. F. (2002), Seismic wave attenuation: Energy dissipation in viscoelastic crystalline solids, *Rev. Mineral. Geochem.*, *51*, 253–290, doi:10.2138/gsrmg.51.1.253.

Cottrell, A. H., and V. Aytakin (1947), Andrade's creep law and the flow of zinc crystals, *Nature*, *160*, 328–329, doi:10.1038/160328a0.

Darwin, G. H. (1879), On the precession of a viscous spheroid and on the remote history of the Earth, *Philos. Trans. R. Soc. London*, *170*, 447–538, doi:10.1098/rstl.1879.0073.

Darwin, G. H. (1880), On the secular change in the elements of the orbit of a satellite revolving about a tidally distorted planet, *Philos. Trans. R. Soc. London*, *171*, 713–891, doi:10.1098/rstl.1880.0020.

Dehant, V. (1987a), Tidal parameters for an inelastic Earth, *Phys. Earth Planet. Inter.*, *49*, 97–116, doi:10.1016/0031-9201(87)90134-8.

Dehant, V. (1987b), Integration of the gravitational motion equations for an elliptical uniformly rotating Earth with an inelastic mantle, *Phys. Earth Planet. Inter.*, *49*, 242–258, doi:10.1016/0031-9201(87)90027-6.

Durham, W. B., and L. Stern (2001), Rheological properties of water ice—Applications to satellites of the outer planets, *Annu. Rev. Earth Planet. Sci.*, *29*, 295–330, doi:10.1146/annurev.earth.29.1.295.

Durham, W. B., W. B. McKinnon, and L. Stern (2005), Cold compaction of water ice, *Geophys. Res. Lett.*, *32*, L18202, doi:10.1029/2005GL023484.

Duval, P. (1978), Anelastic behaviour of polycrystalline ice, *J. Glaciol.*, *21*, 621–628.

Efroimsky, M., and V. Lainey (2007), The physics of bodily tides in terrestrial planets and the appropriate scales of dynamical evolution, *J. Geophys. Res.*, *112*, E12003, doi:10.1029/2007JE002908.

Efroimsky, M., and J. G. Williams (2009), Tidal torques: A critical review of some techniques, *Celestial Mech. Dyn. Astron.*, *104*, 257–289, doi:10.1007/s10569-009-9204-7.

Everhart, E. (1985), An efficient integrator that uses Gauss-Radau spacings, in *Dynamics of Comets: Their Origin and Evolution*, *Astrophys. Space Sci. Libr.*, vol. 115, edited by A. Carusi and G. B. Valsecchi, p. 185, D. Reidel, Dordrecht,Netherlands.

Findley, W. N., J. S. Lai, and K. Onaran (1976), *Creep and Relaxation of Nonlinear Viscoelastic Materials*, 384 pp., Dover, Mineola, N. Y.

Fletcher, N. H. (1970), *The Chemical Physics of Ice*, 271 pp., Cambridge Univ. Press, New York, doi:10.1017/CBO9780511735639.

Gerstenkorn, H. (1955), Über Gezeitenreibung beim Zweikörperproblem, *Z. Astrophys.*, *36*, 245–274.

Glen, J. W. (1955), The creep of polycrystalline ice, *Proc. R. Soc. London, Ser. A*, *228*, 519–538, doi:10.1098/rspa.1955.0066.

Goldreich, P. (1966), Final spin states of planets and satellites, *Astron. J.*, *71*, 1–7, doi:10.1086/109844.

Goldsby, D. L., and D. L. Kohlstedt (2001), Superplastic deformation of ice: Experimental observations, *J. Geophys. Res.*, *106*, 11,017–11,030, doi:10.1029/2000JB900336.

Goodman, D. J., H. J. Frost, and M. F. Ashby (1981), The plasticity of polycrystalline ice, *Philos. Mag. A*, *43*, 665–695, doi:10.1080/01418618108240401.

Gribb, T. T., and R. F. Cooper (1998), Low-frequency shear attenuation in polycrystalline olivine: Grain boundary diffusion and the physical significance of the Andrade model for viscoelastic rheology, *J. Geophys. Res.*, *103*, 27,267–27,279, doi:10.1029/98JB02786.

Haddad, Y. M. (1995), *Viscoelasticity of Engineering Materials*, 279 pp., Chapman and Hall, London.

Jackson, I. (1993), Dynamic compliance from torsional creep and forced oscillation tests: An experimental demonstration of linear viscoelasticity, *Geophys. Res. Lett.*, *20*, 2115–2118, doi:10.1029/93GL02504.

Jackson, I., J. D. Fitz Gerald, U. H. Faul, and B. H. Tan (2002), Grain-size-sensitive seismic wave attenuation in polycrystalline olivine, *J. Geophys. Res.*, *107*(B12), 2360, doi:10.1029/2001JB001225.

Jacobson, R. A., et al. (2006), The gravity field of the Saturnian system from satellite observations and spacecraft tracking data, *Astron. J.*, *132*, 2520, doi:10.1086/508812.

Jellinek, H. H. G., and R. Brill (1956), Viscoelastic properties of ice, *J. Appl. Phys.*, *27*, 1198–1209, doi:10.1063/1.1722231.

Johnson, R. E., and T. I. Quickenden (1997), Photolysis and radiolysis of water ice on outer solar system bodies, *J. Geophys. Res.*, *102*, 10,985–10,996, doi:10.1029/97JE00068.

Karato, S.-I. (2008), *Deformation of Earth Materials: An Introduction to the Rheology of Solid Earth*, Cambridge University Press, Cambridge, U. K.

Karato, S.-I., and H. A. Spetzler (1990), Defect microdynamics in minerals and solid-state mechanisms of seismic wave attenuation and velocity dispersion in the mantle, *Rev. Geophys.*, *28*, 399–423, doi:10.1029/RG028i004p00399.

Kaula, W. M. (1964), Tidal dissipation by solid friction and the resulting orbital evolution, *Rev. Geophys.*, *2*, 661–684, doi:10.1029/RG002i004p00661.

Lee, L. C., and S. J. S. Morris (2010), Anelasticity and grain boundary sliding, *Proc. R. Soc. A*, *466*, 2651–2671, doi:10.1098/rspa.2009.0624.

Lifshits, I. M., and V. B. Shikin (1965), The theory of diffusional viscous flow of polycrystalline solids, *Sov. Phys. Solid State*, *6*, 2111–2118.

MacDonald, G. J. F. (1964), Tidal friction, *Rev. Geophys.*, *2*, 467–541, doi:10.1029/RG002i003p00467.

McCarthy, C. M., and J. C. Castillo-Rogez (2011), Ice Attenuation properties: Application to planetary bodies, in *The Science of Solar System Ices*, edited by M. S. Gudipati and J. C. Castillo-Rogez, Springer, New York, in press.

McCarthy, C., R. F. Cooper, and D. L. Goldsby (2008), Dynamic attenuation measurements of polycrystalline ice at planetary conditions, *Lunar Planet. Sci.*, *39*, 2512.

Melnikov, A. V., and I. I. Shevchenko (2010), The rotation states predominant among the planetary satellites, *Icarus*, *209*, 786–794, doi:10.1016/j.icarus.2010.04.022.

Miguel, M.-C., A. Vespignani, and S. Zapperi (2000), Modeling collective dislocations dynamics in ice single crystals, in *Multiscale Phenomena in Materials: Experiments and Modeling*, *Mater. Res. Soc. Symp. Proc.*, vol. 578, edited by I. M. Robertson et al., pp. 149-154, Mater. Res. Soc., Warrendale, Pa.

Munk, W. H., and G. J. F. MacDonald (1960), *The Rotation of the Earth: A Geophysical Discussion*, Cambridge University Press, Cambridge, U. K.

Nimmo, F. (2008), Tidal dissipation and faulting, paper presented at Science of Solar System Ices Workshop, Lunar and Planet. Inst., Oxnard, Calif.

Oguro, M. (2001), Anelastic behavior of H_2O ice single crystals doped with KOH, *J. Phys. Chem. Solids*, *62*, 897–902, doi:10.1016/S0022-3697(00)00247-X.

Onsager, L., and L. K. Runnels (1969), Diffusion and relaxation phenomena in ice, *J. Chem. Phys.*, *50*, 1089, doi:10.1063/1.1671162.

Parameswaran, V. R. (1987), Orientation dependence of elastic constants for ice, *Def. Sci. J.*, *37*, 367–375.

Peale, S. J. (1977), Rotation histories of the natural satellites, in *Planetary Satellites*, edited by J. A. Burns, pp. 87–112, Univ. of Ariz. Press, Tucson.

Petrenko, V. F., and R. W. Whitworth (1999), *Physics of Ice*, 390 pp., Oxford Univ. Press, New York.

Raj, R. (1975), Transient behaviour of diffusion-induced creep and creep rupture, *Metall. Mater. Trans. A*, *6*, 1499–1509, doi:10.1007/BF02641961.

Raj, R., and M. F. Ashby (1971), On grain boundary sliding and diffusional creep, *Metall. Trans.*, *2*, 1113–1127, doi:10.1007/BF02664244.

Reeh, N., E. L. Christensen, C. Mayer, and O. B. Olesen (2003), Tidal bending of glaciers: A linear viscoelastic approach, *Ann. Glaciol.*, *37*, 83–89, doi:10.3189/172756403781815663.

Ramseier, R. O. (1967), Self-diffusion of tritium in natural and synthetic ice mono-crystals, *J. Appl. Phys.*, *38*, 2553–2556, doi:10.1063/1.1709948.

Robuchon, G., G. Choblet, G. Tobie, O. Cadek, C. Sotin, and O. Grasset (2010), Coupling of thermal evolution and despinning of early Iapetus, *Icarus*, *207*, 959–971, doi:10.1016/j.icarus.2009.12.002.

Romanowicz, B., and J. Durek (2000), Seismological constraints on attenuation in the Earth: a review, in *Earth's Deep Interior: Mineral Physics and Tomography From the Atomic to the Global Scale*, *Geophys. Monogr. Ser.*, vol. 117, edited by S. Karato et al., pp. 161–180, AGU, Washington, D. C.

Shito, A., S.-I. Karato, and J. Park (2004), Frequency dependence of Q in Earth's upper mantle inferred from continuous spectra of body waves, *Geophys. Res. Lett.*, *31*, L12603, doi:10.1029/2004GL019582.

Smith, M. (1974), The scalar equations of infinitesimal elastic-gravitational motion for a rotating, slightly elliptical Earth, *Geophys. J. R. Astron. Soc.*, *37*, 491–526.

Sohl, F., and T. Spohn (1997), The interior structure of Mars: Implications from SNC meteorites, *J. Geophys. Res.*, *102*, 1613–1635, doi:10.1029/96JE03419.

Takeuchi, H., and M. Saito (1972), Seismic surface waves, in *Methods in Computational Physics*, vol. 1, edited by B. A. Bolt, pp. 217–295, Academic, New York.

Tan, B. H., I. Jackson, and J. D. Fitz Gerald (2001), High-temperature viscoelasticity of fine-grained polycrystalline olivine, *Phys. Chem. Miner.*, *28*, 641–664, doi:10.1007/s002690100189.

Tatibouet, J., J. Perez, and R. Vassoille (1981), Very low-frequencies internal-friction measurements of ice I_h, *J. Phys. Colloq.*, *42*, C5-541–C5-546, doi:10.1051/jphyscol:1981582.

Tatibouet, J., J. Perez, and R. Vassoille (1983), Study of lattice-defects in ice I_h by very-low-frequency internal-friction measurements, *J. Phys. Chem.*, *87*, 4050–4054, doi:10.1021/j100244a010.

Tatibouet, J., J. Perez, and R. Vassoille (1987), Study of grain-boundaries in ice by internal friction measurement, *J. Phys. Colloq. C*, *48*, 197–203, doi:10.1051/jphyscol:1987128.

Thomas, P. C., et al. (2007), Shapes of the Saturnian icy satellites and their significance, *Icarus*, *190*, 573–584, doi:10.1016/j.icarus.2007.03.012.

Tobie, G., A. Mocquet, and C. Sotin (2005), Tidal dissipation within large icy satellites: Applications to Europa and Titan, *Icarus*, *177*, 534–549, doi:10.1016/j.icarus.2005.04.006.

Vassoille, R., J. Tatibouet, J. Perez, and P.-F. Gobin (1974), Comportement anelastique de la glace aux faibles frequences de solicitation, *C. R. Acad. Sci., Ser. B*, *278*, 409–412.

Webb, S., and I. Jackson (2003), Anelasticity and microcreep in polycrystalline MgO at high temperature: an exploratory study, *Phys. Chem. Miner.*, *30*, 157–166, doi:10.1007/s00269-003-0299-1.

Wisdom, J., S. J. Peale, and F. Mignard (1984), The chaotic rotation of Hyperion, *Icarus*, *58*, 137–152, doi:10.1016/0019-1035(84)90032-0.

Zschau, J. (1978), Phase shifts of tidal load deformations of the Earth's surface due to low-viscosity layers in the interior, in *Proceedings of the 8th International Symposium on Earth Tides, Held in Bonn on 19–24 September 1977*, edited by M. Bonatz and P. J Melchior, pp. 62–94, Inst. für Theoret. Geod., Univ. Bonn, Bonn, Germany.

J. C. Castillo-Rogez, Jet Propulsion Laboratory, California Institute of Technology, Pasadena, CA 91109, USA. (julie.c.castillo@jpl.nasa.gov)

M. Efroimsky, U.S. Naval Observatory, 3450 Massachusetts Avenue NW, Washington, DC 20392, USA. (michael.efroimsky@usno.navy.mil)

V. Lainey, IMCCE, Observatoire de Paris, UMR 8028 du CNRS, 77 Avenue Denfert-Rochereau, F-75014 Paris, France. (lainey@imcce.fr)